PLANETARY SCIENCE

Geological, multispectral, and meteorological imaging results from the Mars 2020 Perseverance rover in Jezero crater

James F. Bell III[1]*, Justin N. Maki[2], Sanna Alwmark[3,4], Bethany L. Ehlmann[2], Sarah A. Fagents[5], John P. Grotzinger[6], Sanjeev Gupta[7], Alexander Hayes[8], Ken E. Herkenhoff[9], Briony H. N. Horgan[10], Jeffrey R. Johnson[11], Kjartan B. Kinch[3], Mark T. Lemmon[12], Morten B. Madsen[3], Jorge I. Núñez[11], Gerhard Paar[13], Melissa Rice[14], James W. Rice Jr.[1], Nicole Schmitz[15], Robert Sullivan[8], Alicia Vaughan[9], Mike J. Wolff[12], Andreas Bechtold[16,17], Tanja Bosak[18], Louise E. Duflot[14], Alberto G. Fairén[19,8], Brad Garczynski[10], Ralf Jaumann[20], Marco Merusi[3], Chase Million[21], Eleni Ravanis[5], David L. Shuster[22], Justin Simon[2], Michael St. Clair[21], Christian Tate[8], Sebastian Walter[20], Benjamin Weiss[18], Alyssa M. Bailey[1], Tanguy Bertrand[23], Olivier Beyssac[24], Adrian J. Brown[25], Piluca Caballo-Perucha[13], Michael A. Caplinger[26], Christy M. Caudill[27], Francesca Cary[5], Ernest Cisneros[1], Edward A. Cloutis[28], Nathan Cluff[1], Paul Corlies[8], Kelsie Crawford[1], Sabrina Curtis[14], Robert Deen[2], Darian Dixon[26], Christopher Donaldson[26], Megan Barrington[8], Michelle Ficht[26], Stephanie Fleron[29], Michael Hansen[29], David Harker[26], Rachel Howson[26], Joshua Huggett[26], Samantha Jacob[1], Elsa Jensen[26], Ole B. Jensen[3], Mohini Jodhpurkar[1], Jonathan Joseph[8], Christian Juarez[26], Linda C. Kah[30], Oak Kanine[6], Jessica Kristensen[29], Tex Kubacki[26], Kristiana Lapo[14], Angela Magee[26], Michael Maimone[26], Greg L. Mehall[1], Laura Mehall[1], Jess Mollerup[14], Daniel Viúdez-Moreiras[19,31], Kristen Paris[1], Kathryn E. Powell[1], Frank Preusker[15], Jon Proton[32], Corrine Rojas[1], Danny Sallurday[26], Kim Saxton[2], Eva Scheller[6], Christina H. Seeger[6], Mason Starr[26], Nathan Stein[6], Nathalie Turenne[28], Jason Van Beek[2], Andrew G. Winhold[1], Rachel Yingling[26]

Perseverance's Mastcam-Z instrument provides high-resolution stereo and multispectral images with a unique combination of spatial resolution, spatial coverage, and wavelength coverage along the rover's traverse in Jezero crater, Mars. Images reveal rocks consistent with an igneous (including volcanic and/or volcaniclastic) and/or impactite origin and limited aqueous alteration, including polygonally fractured rocks with weathered coatings; massive boulder-forming bedrock consisting of mafic silicates, ferric oxides, and/or iron-bearing alteration minerals; and coarsely layered outcrops dominated by olivine. Pyroxene dominates the iron-bearing mineralogy in the fine-grained regolith, while olivine dominates the coarse-grained regolith. Solar and atmospheric imaging observations show significant intra- and intersol variations in dust optical depth and water ice clouds, as well as unique examples of boundary layer vortex action from both natural (dust devil) and Ingenuity helicopter–induced dust lifting. High-resolution stereo imaging also provides geologic context for rover operations, other instrument observations, and sample selection, characterization, and confirmation.

INTRODUCTION

The NASA Mars 2020 Perseverance rover landed in Jezero crater (18.4446°N, 77.4509°E) on 18 February 2021. Jezero is a ~45-km-diameter impact crater of mid- to late-Noachian age (~3.7 to 4.1 billion years) located on the northwest rim of the ~1200-km-diameter Isidis impact basin (Fig. 1). A major goal of the mission is to characterize the geology of Jezero crater and its neighboring areas, to improve our understanding of Martian crustal processes and past climates, and to search for evidence of possible ancient Martian life. To address these questions, Perseverance will collect up to 38 rock and regolith samples to be returned for analysis in Earth laboratories as part of the NASA/European Space Agency (ESA) Mars Sample Return campaign. For these samples to have scientific value, contextual documentation of local and regional sedimentary and igneous textures and geologic structures that reveal petrogenesis is essential for elucidation of their origin and evolution. Observations by the rover's Mast Camera Zoom (Mastcam-Z) instrument (1),

which provide a unique combination of spatial resolution, spatial coverage, and wavelength coverage from the rover, are central to characterizing and documenting the geology of Perseverance's field site, and to placing the geochemical and mineralogic data collected by other instruments in context.

This paper reports Mastcam-Z geologic observations conducted during the first Earth year of operations (up to ~sol 355), devoted primarily to investigating crater floor rocks near the Octavia E. Butler (OEB) landing site. Before landing, multiple hypotheses were developed for the origin of these rocks, including formation by both sedimentary and igneous processes [e.g., (2–8)]. This paper emphasizes crater floor rock morphologies and stratigraphy, including textures and multispectral properties. Initial remote sensing and in situ data from Perseverance's integrated instrument suite indicate an igneous origin for the crater floor rocks (9). This paper presents properties of these materials observed by Mastcam-Z to provide necessary context of the large-scale geometry of the floor units and to provide

the macroscale geologic and mineralogic evidence to support an igneous interpretation. In addition, the results reported here enhance and augment the initial fluvio-deltaic discoveries about Jezero's western fan deposits (10) by substantially extending the high-resolution imaging coverage of the stratification exposed in the fan's distal scarp. Furthermore, these observations enable the characterization of the regolith and the current atmospheric environment, important both for local and regional scientific context and for planning of future human missions.

Mastcam-Z is a novel pair of variable focal length multispectral charge-coupled device (CCD) cameras used by the Perseverance rover team to document the color, size, shape, texture, and spectral properties of rocks and soils, and the properties and behavior of dust and ice aerosols in the boundary layer and the sky above the crater (see Materials and Methods for more details on the cameras and calibration and processing of their imaging data). These cameras provide a unique combination of wavelength range, high spatial resolution, and variable field of view for extensive landscape coverage, compared to other rover instruments. Their matched focal length ranges, plus the unprecedented downlink data volume from the mission so far that has been enabled by substantial NASA and ESA investments in Mars orbiter communications relay infrastructure, have also allowed almost all Mastcam-Z images to be collected in stereo, enabling detailed three-dimensional (3D) interpretations of outcrop topology at the fine (millimeter to centimeter to decimeter) scales required for precise stratigraphic mapping in the near field and at greater observation distances than other imaging systems on the rover. The resulting derived shapes, topographic relationships, and digital terrain models (DTMs) substantially enhance understanding of the stratigraphic relationships and overall geologic context of the surface materials encountered.

The wavelength coverage of Mastcam-Z multispectral observations (442 to 1022 nm) spans key diagnostic spectral regions not possible to observe with other rover instruments. Specifically, observations and results reported here derived from 465- to 540-nm and 850- to 1022-nm reflectance measurements provide more effective remote sensing constraints on relevant ferric and ferrous mineralogies than possible with other instruments. This unique wavelength coverage enables the detection and spatial mapping of important differences in primary mafic mineralogy (e.g., olivine and pyroxene) as well as of secondary minerals associated with widespread alteration (e.g., hematite and other ferric oxyhydroxides).

Multispectral and stereoscopic images, together with derived data products and visualizations, allow the rover team to observe and characterize the crater and its geologic and meteorologic context from three different spatial perspectives. First, rover-scale observations at close range provide details of morphologic, topographic, structural, stratigraphic, textural, multispectral, and photometric details of rocks, outcrops, and regolith at the OEB landing site, and along the rover's ~2.9-km traverse within the outcrop areas of the Máaz and Séítah formations. The provisional names of formations, members, and sampling sites along the rover's traverse in Jezero crater are from (9) and were thematically based on the names of the traversed quadrangles mapped before landing: Canyon de Chelly and Verdon (4). These broken-up, boulder-dominated, and variably regolith-covered terrains correspond to the dark unit with lobate margins that has been previously mapped from orbit as the "crater floor–fractured rough (Cf-fr)" unit (2) and are now collectively known in situ as the "Maaz formation" (9). In addition, what is now referred to as the "Seitah formation" was mapped from orbit as the "crater floor fractured 1" unit (2). These observations play an important role in the identification of a variety of geologically diagnostic rock types, landforms, and surface compositions, as well as in sample site selection, with Mastcam-Z images used in sample extraction, caching verification, and sample documentation activities.

Second, distant observations, from a few kilometers out to the crater rim and beyond at 10- to 40-km distances (Fig. 1), show details of Jezero's western delta, its erosional remnants, and other hills, buttes, fan deposits, impact craters, and the looming crater rim itself, providing context for the materials and units that the rover is exploring directly, including the rock and regolith samples being collected for eventual return to Earth.

Third, surface-atmosphere interactions, current meteorological conditions, and dynamic processes and events are assessed with a rich dataset acquired at an unprecedented cadence of intra- and intersol solar and atmospheric imaging observations, including images and videos of the horizon, Sun, sky, and Martian satellites. The Mastcam-Z atmospheric observations and results reported here provide the highest temporal resolution image-based monitoring of the Martian environment to date. This includes the only estimates of atmospheric opacity in both the visible and short-wave near infrared (IR), important for constraining dust physical and radiative properties; the first reported observations and interpretations of ice clouds in Jezero crater; and the first reporting of interesting and important surface-atmosphere boundary layer effects caused by the Ingenuity helicopter (used to uniquely probe the mechanics and dynamics of dust lifting and transport).

In addition, Mastcam-Z data products described here also provided operational support and scientific context for rover navigation, observations using the rover arm, sample selection and core characterization, and observations by other rover instruments/systems. An example of the latter is videos of Ingenuity helicopter activities.

[1]School of Earth and Space Exploration, Arizona State University, Tempe, AZ 85281, USA. [2]Jet Propulsion Laboratory, California Institute of Technology, Pasadena, CA 91109, USA. [3]Niels Bohr Institute, University of Copenhagen, 2100 Copenhagen, Denmark. [4]Department of Geology, Lund University, 22362 Lund, Sweden. [5]Hawai'i Institute of Geophysics and Planetology, University of Hawaii, Honolulu, HI 96822, USA. [6]California Institute of Technology, Pasadena, CA 91125, USA. [7]Department of Earth Science and Engineering, Imperial College London, London, UK. [8]Department of Astronomy, Cornell University, Ithaca, NY 14850, USA. [9]USGS Astrogeology Science Center, Flagstaff, AZ 86001, USA. [10]Department of Earth, Atmospheric, and Planetary Sciences, Purdue University, West Lafayette, IN 47907, USA. [11]Johns Hopkins University Applied Physics Laboratory, Laurel, MD 20723, USA. [12]Space Science Institute, Boulder, CO 80301, USA. [13]Joanneum Research, Graz 8010, Austria. [14]Western Washington University, Bellingham, WA 98225, USA. [15]German Aerospace Center (DLR), Berlin 12489, Germany. [16]Department of Lithospheric Research, University of Vienna, 1090 Vienna, Austria. [17]Austrian Academy of Sciences, Vienna 1010, Austria. [18]Department of Earth, Atmospheric and Planetary Sciences, Massachusetts Institute of Technology, Cambridge, MA 02139, USA. [19]Astrobiology Center (CSIC-INTA), Madrid, Spain. [20]Institute for Geological Sciences, Freie Universitaet Berlin, 14195 Berlin, Germany. [21]Million Concepts LLC, Louisville, KY 40203, USA. [22]Department of Earth and Planetary Science, University of California, Berkeley, Berkeley, CA 94720, USA. [23]NASA/Ames Research Center, Moffett Field, CA 94035, USA. [24]Institut de Minéralogie, Physique des Matériaux et Cosmochimie, CNRS, Muséum National d'Histoire Naturelle, Sorbonne University, Paris 75005, France. [25]Plancius Research, Severna Park, MD 21146, USA. [26]Malin Space Science Systems Inc., San Diego, CA 92121, USA. [27]University of Western Ontario, London, ON N6A 3K7, Canada. [28]University of Winnipeg, Winnipeg, MB R3B 2E9, Canada. [29]University of Copenhagen, Copenhagen 1165, Denmark. [30]Department of Earth and Planetary Sciences, University of Tennessee, Knoxville, TN 37916, USA. [31]National Institute for Aerospace Technology, Madrid, Spain. [32]Opscode LLC, Healdsburg, CA 95448, USA.
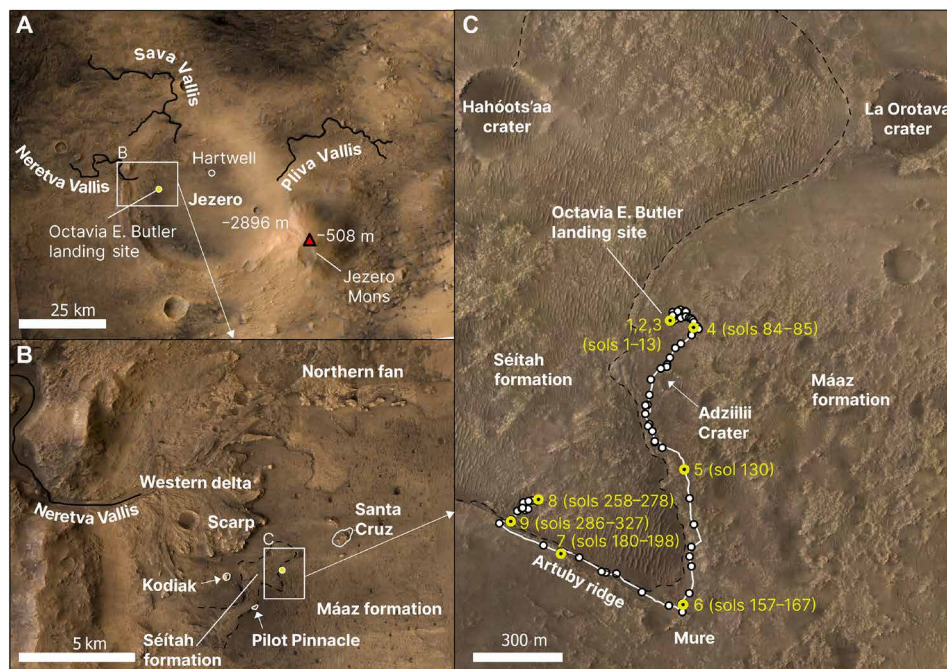*Corresponding author. Email: jim.bell@asu.edu

Fig. 1. Jezero crater context and traverse region. Overview map of the Mars 2020 Perseverance landing site and its regional context. North is up, and illumination is from the left. (**A**) Context map showing Jezero crater, the inlet/outlet channels (outlined in black), and the edifice Jezero Mons in the southeast. (**B**) Close-up of the western delta with its associated features as mentioned in the text. (**C**) Detail view of the rover landing and traverse site, through mission sol 327 (20 January 2022). White circles represent the sol-by-sol locations of the rover starting from the OEB landing site, and yellow circles represent the different site locations defined so far in the mission. Base images: MRO/HiRISE, MRO/CTX, MEx/HRSC.
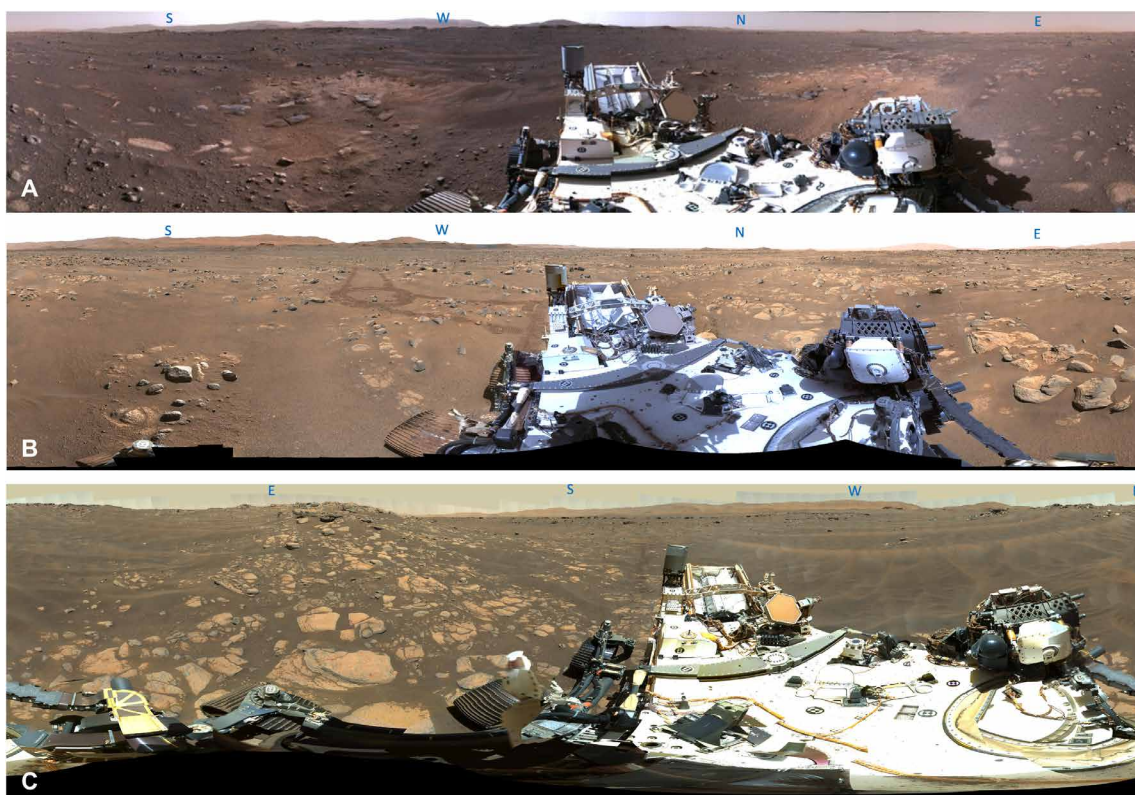

Fig. 2. Example 360° mosaics. Mastcam-Z enhanced color RGB 360° panorama from the Perseverance rover. (**A**) OEB landing site, 34-mm focal length, sol 3. (**B**) Van Zyl Overlook, 110-mm focal length, sols 53 to 64. (**C**) Village outcrop, within Séítah, 110-mm focal length, sols 214 to 215. Cylindrical projection views with local azimuth cardinal points indicated and extending from −60° local elevation angle out to the horizon.

RESULTS

Rover-scale physiography of Jezero crater

Observations by Mastcam-Z have characterized the geology of the landing site, observing a range of rock morphologies and compositions along the rover path and in more distant areas. Initial panoramic views of the OEB landing site (Fig. 2) show a generally low-relief plain that extends ~100 m around the rover in all directions. This local plain consists of regolith interspersed with rocks exhibiting light-toned, low-relief, skyward-facing surfaces that express themselves with a fitted fabric, similar to paver stones. These rocks (Figs. 2 and 3 and fig. S1) commonly exhibit polygonal fracture patterns, indicating that the fracturing occurred in place; thus, the exposed rocks and associated underlying bedrock are also likely in place. Rock surfaces with higher relief (typically <30 cm; see Materials and Methods for details on topography and DTM generation from stereo imaging) commonly exhibit darker tones and are scattered on the local plain around the landing site. Scouring from the Mars 2020 sky crane landing system's terminal descent engines at two areas adjacent to the rover's touchdown point exposed darker-toned rock surfaces that had been at least partly covered by regolith. Removal of the brighter material from these rocks by exhaust impingement and the exposure of more pitted surfaces compared to nearby pavers that were not impinged implies that the bright covering or coating material was not strongly adhered to these darker rock surfaces and is instead a loose mantle deposited onto rather than derived from weathering of these rocks. In contrast, bright surfaces on some pavers (e.g., the rock named Máaz) withstood the brunt of the descent plumes (see, for example, the EDL video publicly released by NASA at https://mars.nasa.gov/mars2020/multimedia/videos/?v=461, specifically the surface imaging starting around time stamp 2 min and 40 s). That, plus the darker interiors of abrasion patches like Guillaumes on Máaz-class rocks (e.g., fig. S3), suggests that this bright material is strongly adhered to the rock surface and thus could be an alteration rind or coating.

At ranges >100 m from the OEB landing site, clusters of darker-toned boulders and rubble-forming low hummocks or short ridges rise 1 to 3 m above the plain. Higher spatial resolution near-field views reveal dark-toned and fractured or jointed rock outcrops and boulders exhibiting variably massive (structureless at centimeter scales), pitted, wind-abraded textures but no substantial evidence of pronounced stratification (Figs. 3 and 4). Erosion of some rock outcrops is occurring in place, forming ridge crests that are smooth (at centimeter scales) and rounded boulders that have not been transported from their sites of formation. Other boulders are more angular, isolated, and high standing in the terrain (perhaps distant impact ejecta "float" and/or ventifacts; e.g., Figs. 3 and 4), and still others are subrounded to rounded and high standing (typically ~30 to 50 cm) but connected to underlying, lighter-toned pavers (Fig. 3A). Textural, multispectral, and elemental (11) measurements support the hypothesis that the pavers and their overlying high-standing rocks are compositionally similar. Aeolian bedforms several meters long, many with flat topped crests up to 20 cm high, are sparsely distributed near the landing site (Fig. 4), and some of the regolith between and among the ridges and boulders consist of aeolian ripples, some of which partially bury or embay rocks and pavers.

More distant features include the southeast-facing scarp of the Jezero western delta (Fig. 5), which rises ~70 to 90 m above the elevation of the landing site and extends along its length from ~2.0 to 6.0 km from OEB. Prominent buttes of similar height named Pilot Pinnacle (~2.0 km southwest) and Kodiak (~2.3 km west) and another prominent ~50-m high butte called Santa Cruz (~2.6 km east) have been interpreted to be remnants of the eroded Jezero fluvio-deltaic-lacustrine sedimentary system [e.g., (2–5, 10)]. Other more distal hills and buttes are identified in high-resolution images, extending many tens of kilometers southwest across the floor of Jezero; some, especially cone-like features inside the southwest rim of the crater (fig. S2F), could potentially be of volcanic origin based on their morphology and chain-like alignment [e.g., (12, 13)].
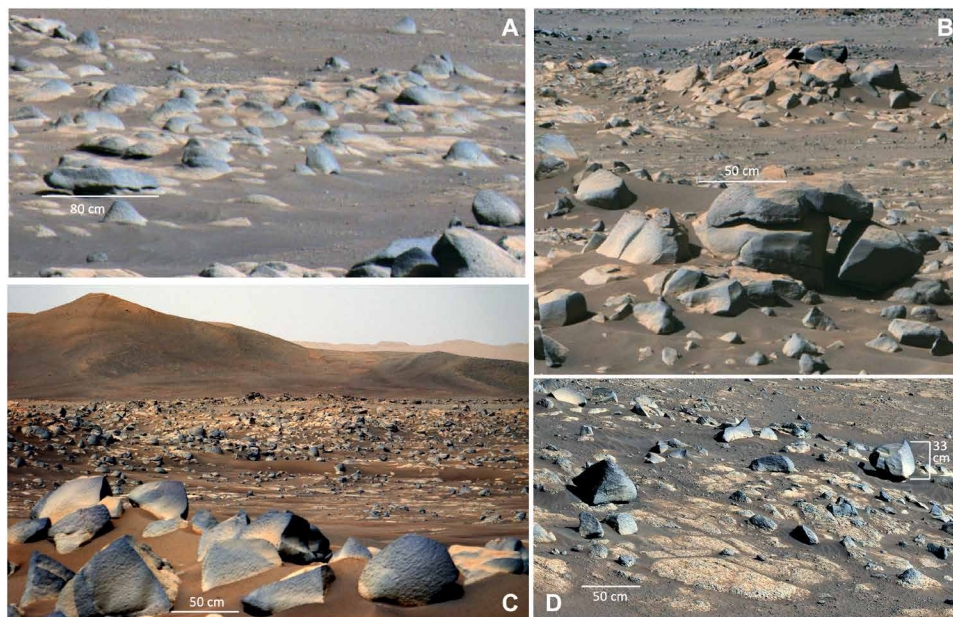
Fig. 3. Examples of typical Máaz formation rocks. (**A**) Naat'áanii pavers and associated higher-standing Ch'ał member rocks. Sol 22, sequence zcam07000. (**B**) Ch'ał member rocks. Sol 63, zcam08108. (**C**) Field of typical Ch'ał member boulders, looking northeast toward Santa Cruz hill. Sol 68, zcam8028. (**D**) Roubion member pavers and Ch'ał member rocks. Sol 135, zcam08139.
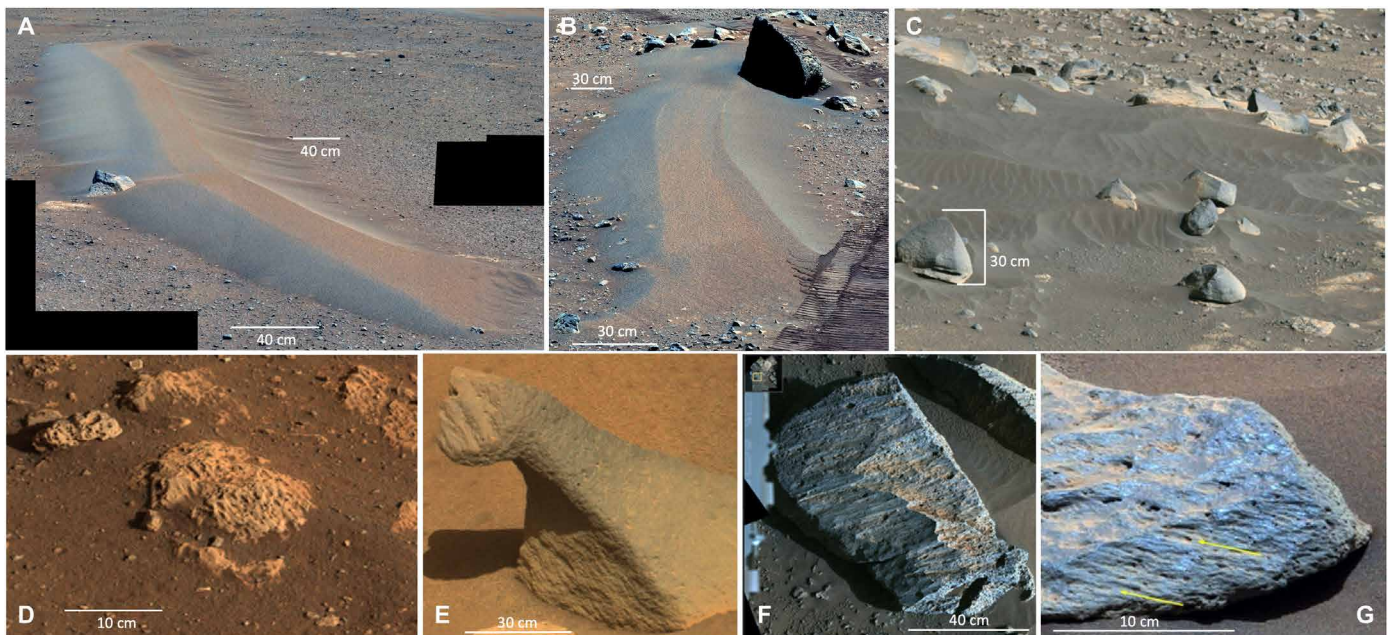
Fig. 4. Examples of aeolian regolith deposits and wind-carved rock surfaces in Jezero crater. (**A**) from sol 113, zcam08084 and (**B**) from sol 123, zcam08119 show examples of 15- (A) and 5-m-long (B) and 15- to 20-cm-tall Máaz terrain aeolian bedforms with flat-topped 2.3-m (A) and 1.3-m (B) wide crests. (**C**) Example of typical dark-toned aeolian sands that have moved over Máaz formation rocks (sol 135, zcam08139). (**D** to **G**) Examples of Máaz formation rocks with wind abrasion textures, interpreted as ventifacts: (D) Unnamed target from the landing site, sol 3, aut_04096. (E) Example 16-cm-tall rock from Van Zyl Overlook, sol 54, zcam08101. (F) The 60-cm-long rock Rochette from sol 181, zcam08199. (G) Example of wind-abraded flute orientations measured (yellow lines) using Mastcam-Z stereo observations of an unnamed 13-cm-wide rock on sol 180, zcam08194 (see also Materials and Methods).
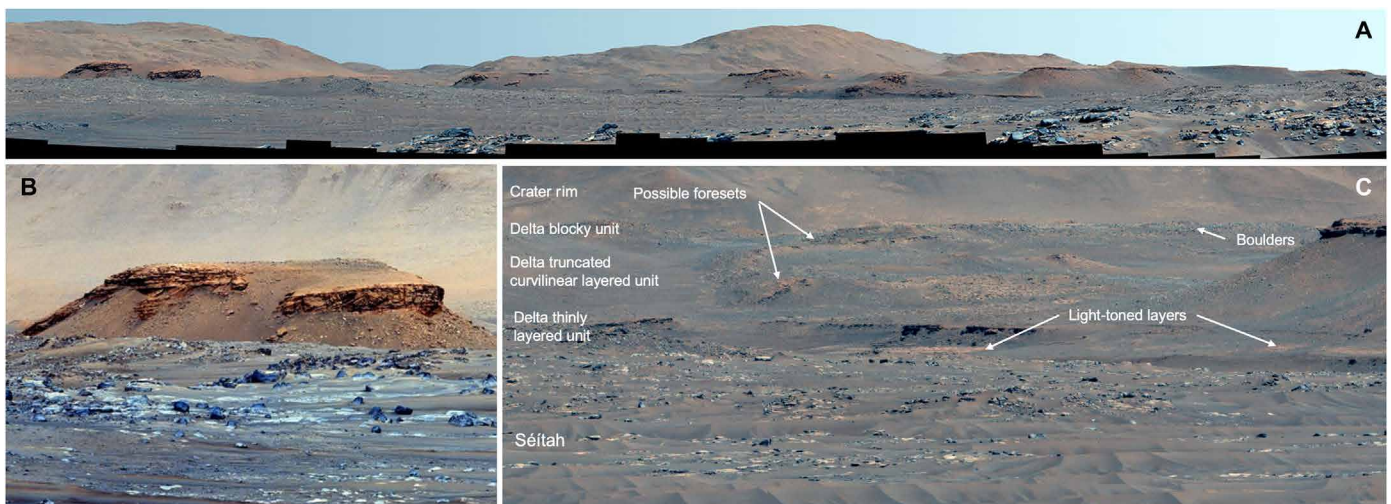

Fig. 5. Morphology of the Jezero western delta scarp and remnants. (**A**) Mastcam-Z enhanced color panorama looking toward the scarp at the easternmost extent of the Neretva Vallis fan delta. View is from the west (left) to the north (right), from a location near site position 8 within Séítah. In the foreground, layered rocks of Séítah and ripple-dominated landscape are visible. In the distance, the hummocky, terraced crater rim is exposed, with smaller craters and exposures of light-toned beds. The highest part of the rim is ~9.6 km distant and ~800 m higher in elevation above the crater floor viewpoint. Sol 275, zcam08292. (**B**) Kodiak butte, a putative delta remnant (10), showing subhorizontal and inclined beds (sol 63, zcam08022). The butte is ~2.4 km distant; the top of the plateau is ~130 m wide and rises ~77 m above the crater floor, and the sedimentary rock packages exposed here are ~10 m thick. (**C**) Zoomed-in view of the center of (A) showing the delta blocky and delta truncated curvilinear layered units in the "Hawksbill gap" region. The part of the delta scarp exposed here is ~2.3 km distant. In the foreground, Séítah formation rocks are visible in the ripple-dominated landscape.

The rims and/or ejecta blocks from several large impact craters on the floor of Jezero can also be identified in high spatial resolution images, including 70-m-diameter Adziilii crater (190 m to the south of OEB; fig. S2A), 325-m-diameter La Orotava crater (930 m to the northeast), and 1.8-km-diameter Hartwell crater (15 km to the northeast).

The viewshed of the most distant visible features from the landing site provides context for the observations along the traverse route. The concave-sloped inner walls of the rim of Jezero crater at 10- to 40-km distance rise from 800 to 1200 m above the crater floor and exhibit light-toned layers, terraces, smaller craters, and evidence for downslope motion of dust and/or debris at meters to tens of meters scale. Also visible are the mouth and fan delta scarps of Sava Vallis (fig. S2, B and E), the northern channel interpreted to have transported fluid and sediment into Jezero crater 7.5 to 8 km away, the mouth of Neretva Vallis (fig. S2C) that intersects Jezero crater from the west ~10 km westward, and the overflow channel Pliva Vallis (fig. S2D) that is incised into the eastern rim ~36 km away from the landing site [e.g., (2–5)]. One of the most distant visible features are the upper slopes of a large conical mountain (Jezero Mons) outside of Jezero crater 47 km to the east-southeast of OEB and rising ~2 km above the crater rim (fig. S2G). Its morphology in orbital (5, 8) and Mastcam-Z distant surface imaging is consistent with it potentially being a volcanic edifice. Alternately, it could be an erosional remnant of the slumped once-higher crater wall [e.g., (5, 13)], with an irregularly shaped summit depression formed by an impact.

A variety of diagnostic rock outcrop morphologies were characterized as the rover traversed along the western edge of the landing site plains (Máaz formation). This route was chosen to allow the rover to enter the neighboring Séítah region, which potentially contains the oldest rocks on the crater floor [e.g., (2)]. The diversion around the southern tip of Séítah was required because its margin is partly defined by large, mostly nontraversable aeolian bedforms (Figs. 1C, 2C, and 5C). Perseverance was able to enter Séítah ~1 km southwest of the landing site. As described below and elsewhere (9, 11), Máaz and Séítah are composed of markedly different rock types, in terms of both their geologic expression and geochemical/mineralogic character.

Geologic observations and results
Crater floor rock and outcrop morphologies, textures, and multispectral properties
Mastcam-Z observations of bedrock exposed on the crater floor are critical to defining the macroscale textures, structure, and stratigraphy of the crater floor rocks. On the basis of these observations, the strata have been assigned to the Máaz and Séítah formations (9). The pyroxene-bearing Máaz formation has been subdivided into five members (Ch'ał, Naat'áanii, Rochette, Artuby, and Roubion), and the variably olivine-bearing Séítah formation includes two members encountered to date (Bastide and Content). Table 1 provides an overview of the names and other characteristics of the Jezero crater floor formations, members, outcrops, and sampling sites described here.

Máaz formation observations. Near the landing site, the Máaz formation is dominated by two rock morphologies: angular to rounded and apparently unlayered boulder-forming bedrock of the Ch'ał ember, and flat, polygonal bedrock pavers of the Naat'áanii member. These rocks overlie the stratified rocks of the Rochette and Artuby members of the Máaz formation (9), which are best exposed along the Artuby ridge and characterized by distinct layering (Fig. 6), and the flat-lying Roubion member pavers. The Artuby member is defined by repeating layers that alternate in their degree of friability and thickness. Recessive, thin (2 to 10 cm thick) strata repeat in the lower parts of outcrops along the Artuby ridge. The Rochette member, exposed at the top of the Artuby ridge, comprises massive cap rocks along Artuby ridge, which often show partings or horizontal

Table 1. Relative stratigraphy [based on (9)] of investigated crater floor rocks with formation and member names alongside workspace, abrasion patches, and sample names. Px, pyroxene; Plag, plagioclase; Ol, olivine.

| Formation	Member	Workspace or outcrop	Abrasion patch	Core samples acquired	Key characteristics	Key mineralogy*	Relevant figures
Máaz	Ch'ał	Sid	Alfalfa	Hahonih and Atsah	Massive	Px + Plag	Figures 3 (A to D) and 8B
	Naat'áanii	OEB landing, Naltsos	Not abraded	Not sampled	Flat-lying	Px + Plag	Figures 3 (A and D) and 8C
	Rochette	Citadelle	Bellegarde	Montagnac and Montdenier	Massive, jointed, pitted	Px + Plag	Figures 4F, 6 (D and E) 7 (B to E), and 8D and figs. S3C and S8 (A to C)
	Artuby	Artuby ridge (incl. Grasse)	Montpezat	Not sampled	Distinctly layered	Px + Plag	Figures 6 (A to C) and 8E and fig. S4
	Roubion	Roubion	Guillaumes	Unsuccessful sampling	Flat-lying, friable	Px + Plag	Figure 8F and fig. S3B
Séítah	Content	Hotel	Not abraded	Not sampled	Structureless, pitted	Px + Plag	Figures 6A and 8H and fig. S6D
	Bastide	Issole	Quartier	Robine, Malay	Strongly layered	Ol + Px + Plag	Figure S8 (G to I)
		Brac	Garde	Salette, Coulettes	Strongly layered	Ol + Px + Plag	Figures S3D, S6 (A and D), and S8 (D to F)
		Bastide	Dourbes	Not sampled	Strongly layered	Ol + Px + Plag	Figure 8G and figs. S3E, S5, S6 (A to D), and S7C

*Based on (9, 15).
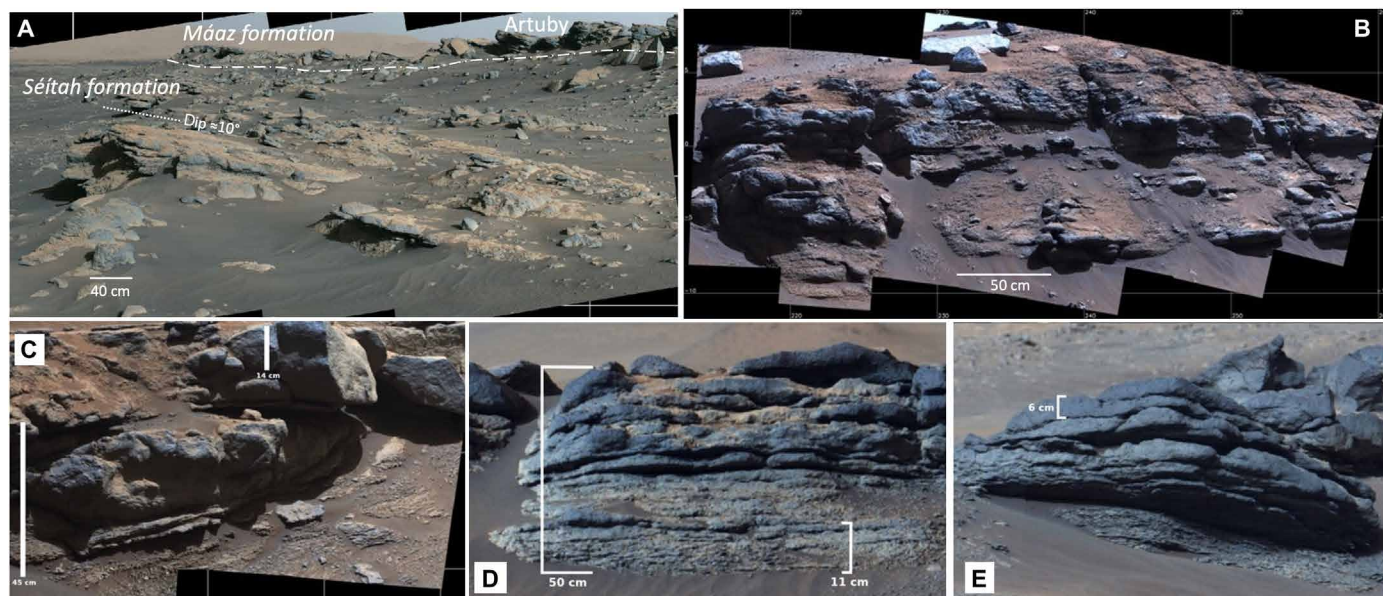
Fig. 6. Examples of massive or thickly layered outcrops to thinly layered outcrops at Artuby ridge. (**A**) Mastcam-Z sol 289 110-mm mosaic of part of the contact along Artuby ridge between the Artuby member of the Máaz formation and the more finely layered rocks of the stratigraphically lower Séítah formation. The average dip of the layers here is ≈10° to the southwest (see Materials and Methods). (**B**) Variations in and transitions between layers of the Artuby ridge at the Grasse outcrop. This outcrop displays several examples of variations between resistance to weathering and the knobby nature of some of the Artuby member layers (especially on the left side). Sol 177, zcam08189. (**C**) Transition from rounded massive/pitted rock morphologies to fine-scale layering among Mure outcrops of the Artuby member. Sol 169, zcam08181. (**D** and **E**) Examples of transitions from decameter-scale to centimeter-scale layering in outcrops within the Rochette member along the Artuby ridge, sol 288, zcam08312.
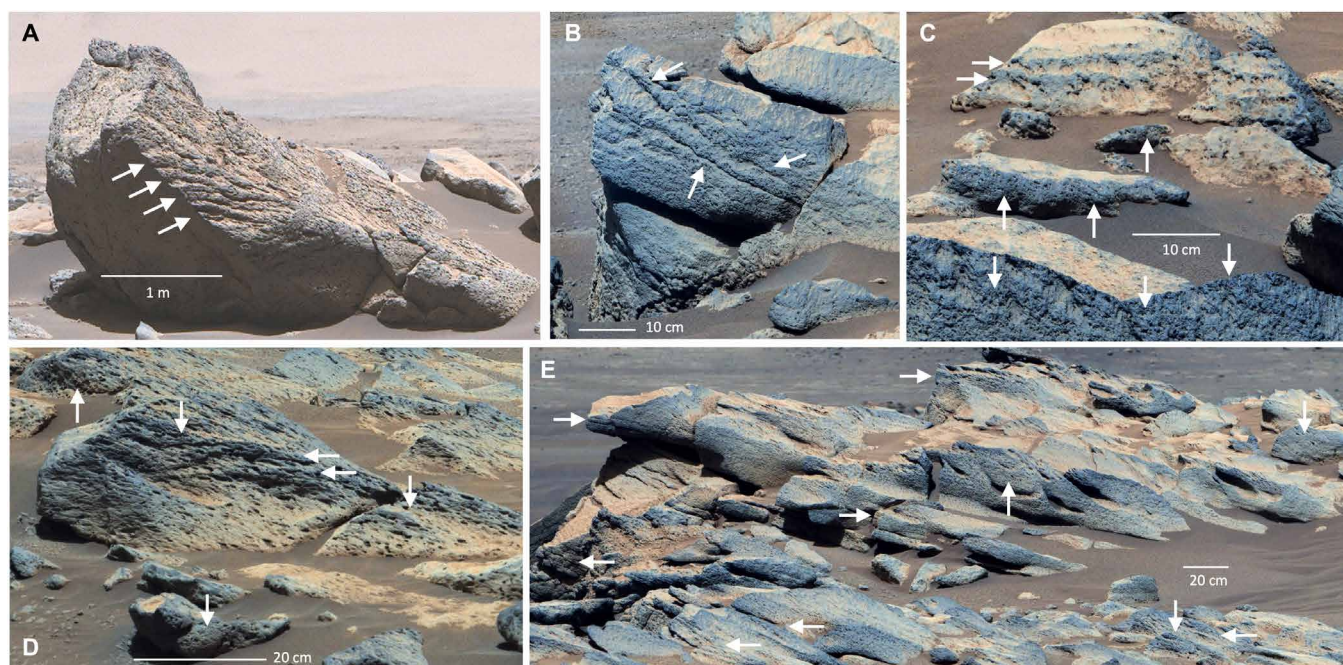

Fig. 7. Máaz formation rocks showing textures reminiscent of lava flows. (**A**) Ropy pahoehoe-like flow textures (starting at arrows) on large ~1.5-m-high and ~4-m-wide boulder (potentially impact ejecta) near Adziilii Crater from sol 110 sequence zcam03159. (**B** to **E**) Examples of morphologies from rocks and outcrops of the Rochette member of the Máaz formation that are consistent with lava flows. These examples are from the Citadelle region of the Artuby ridge. Sol 180 sequences zcam08195 and zcam08196. (**B**) Apparent flow banding (contorted layering with lack of lateral continuity; arrows) in outcrop rock. (C to E) Examples of apparent vesicular textures (vertical arrows) and flow foliation (horizontal arrows) in Jezero floor outcrop rocks.

fractures. While all Máaz rocks show pitting at various scales, some large boulders within the Ch'ał member and resistant massive caprock at the Mure outcrop also show curvilinear patterns of larger voids [e.g., Figs. 7 and 8H and (9)].

Multispectral observations of most members of the Máaz formation exhibit relatively flat spectra from 754 to 1022 nm, often with weak bands near 866 nm indicative of minor hematite. Abraded rock surfaces in the Máaz formation (e.g., Bellegarde; fig. S3) exhibit red patches with relatively strong absorptions near 528 and 866 nm, consistent with a greater abundance of fine-grained, crystalline hematite relative to rock surfaces. Less-dusty surfaces of some Máaz formation rocks, most commonly within the Ch'ał member, exhibit spectra with broad near-IR absorptions centered near 910 nm and with reflectance peaks near 754 nm, consistent with orthopyroxene, orthopyroxene-clinopyroxene mixtures, and some ferric alteration minerals (e.g., Fe^{3+}-bearing phyllosilicates). Subtle variations in the positions, widths, and shapes of these bands suggest that multiple mineral phases are present in varying concentrations or grain sizes between outcrops.

Layered outcrops of the Artuby member exhibit reddish spectral slopes from 442 to 754 nm and broad absorptions between 866 and 910 nm that are similar to, but weaker than, those in the Ch'ał member. The Artuby member layers are distinct from the overlying resistant cap of the Rochette member, which exhibits a distinct spectral flattening between 605 and 754 nm along with either a broad absorption centered between 910 and 939 nm or a shallow, negative slope from 800 to 1022 nm, which are most consistent not only with clinopyroxene but also with some basaltic glasses (Fig. 8). Olivine signatures are not detected within the Máaz formation.

Séítah formation observations. The Séítah formation is exposed to the west and south of the landing site in an erosional window (Fig. 1). Rocks of the formation show distinct olivine-rich/carbonate spectral signatures observed from orbit [see review in (2)]. At the base of the Artuby ridge, stratified Máaz formation rocks overlie thinner bedded (~2 to 10 cm), similarly inclined rocks of the Séítah formation, which typically crop out as variably resistant strata (Fig. 6 and figs. S4 and S5), as well as some apparently structureless or massive variations. Séítah outcrops are characterized by a series of 1- to 10-m-tall northeast-southwest trending bedrock ridges partially covered by aeolian bedforms (Fig. 1 and fig. S6). The Séítah formation ridges are characterized by centimeter-thick layered rocks that occur toward the base of the ridges and are overlain by tens of centimeter-thick massive cap rocks with a tabular geometry. These rocks comprise the Bastide member, formed of strata ~1 to 3 cm thick with tabular morphology and planar to undulating bed bounding surfaces (e.g., figs. S5 and S6). The beds show even thicknesses laterally and are less resistant than the overlying massive cap rocks, resulting in some outcrops with exposed overhangs or others with stair-step patterns (Fig. 6 and fig. S6). The massive cap rocks exhibit beds with thicknesses ranging from ~10 to 50 cm with predominantly tabular geometries. The massive rocks appear to fracture along preexisting horizontal planes. Close-up observations of rock textures of the Bastide member, including at abrasion patches (figs. S3, S4, and S6), indicate that the rocks consist of densely packed, well-sorted, coarse-grained (1 to 2 mm diameter) dark gray angular to subrounded grains/crystals that are surrounded by a lighter-toned material between the grains (9). Reddish brown material is found at grain boundaries and triple junctions, as well as enclosing the light-toned grains.

In some locations, overlying the massive cap rocks, there is a unit composed of loose, pitted decimeter-sized boulders and in-place bedrock (fig. S6) that lacks the olivine signature characteristic of the Bastide member (9). This unit has been designated the Content member (9). Content member rocks are characterized by elongated millimeter- to centimeter-sized pits and lack the bedding characteristic of the Bastide member (Fig. 8H).

In multispectral observations, the Bastide member rocks of the Séítah formation exhibit steep, negative spectral slopes longward of 677 nm, consistent with the broad absorption centered near 1000 nm in olivine (Fig. 8G). The strongest olivine-like features are detected in the abraded regions and drill tailings associated with the Garde and Dourbes targets (Fig. 8A and fig. S3). SuperCam, PIXL, and SHERLOC observations confirm the presence of olivine and pyroxenes with some alteration to carbonates and other phases (9, 14, 15). Such features are absent in the spectra of the pitted rocks comprising the Content member (Fig. 8H). Some abraded or natural rock surfaces exhibit relatively strong absorptions near 528 and 866 nm as well as a neutral or positive near-IR spectral slope, consistent with crystalline hematite. Spectra of the pitted rocks of the Content member have reflectance peaks at 754 nm and broad absorptions centered at 910 nm, consistent with orthopyroxene, and suggesting a distinct olivine-poor composition compared to other Séítah rocks encountered so far.

Coating observations. Discontinuous rock coatings, with purple hues and variable thickness (thicker in millimeter- and centimeter-scale depressions on rock surfaces), are common across all rock morphologies in the Séítah and Máaz formations (e.g., fig. S7). Morphologic evidence, supported by WATSON and SuperCam RMI images [e.g., (11)], suggests that the coatings formed after these rocks were exposed at the Martian surface and have since been exposed to wind abrasion that has variably removed some of the coating. These coatings exhibit absorptions near 528 nm and near 866 to 910 nm, which are consistent with more crystalline hydrated ferric oxides or other hydrated alteration phases (e.g., fig. S7). Multiple time-of-sol observations also reveal large spectral variations of rocks and soils as a function of phase angle. In particular, the purple-hued coatings are more pronounced in images acquired at lower phase angles, which emphasize differences in Máaz formation rocks possibly related to differences in burial/exhumation histories: Brighter-toned rocks exhibit partially dusted or indurated surfaces, and darker-toned rocks are less dusty, with more pristine textures.

Core sample imaging observations. Mastcam-Z has imaged each of the sample cores acquired through sol 337 (9). These images (fig. S8) show the sample in the coring bit before the sample tubes are transferred to the Sample Handling Arm for sealing and storage. These images detail the range of textures and colors present within and among the acquired samples and can be compared to their corresponding abrasion surfaces that are well documented by the full suite of chemical/mineralogic rover instrumentation (fig. S3). The cleaved ends of cores Montdenier and Montagnac and the associated abraded rock outcrop target Bellegarde from the Máaz formation exhibit matching textures of relatively fine-grained (~0.2 to 0.5 mm) interlocking dark-toned and light-toned minerals, consistent with a holocrystalline igneous rock (e.g., fig. S8A of the Rochette samples). The shape and color of the dark-toned mineral grains are consistent with the Mastcam-Z pyroxene spectra commonly seen in Máaz formation rock surfaces (e.g., Fig. 8). Many of the primary mineral grains exhibit variable amounts of brown staining along their edges, consistent with iron oxides, and especially evident around
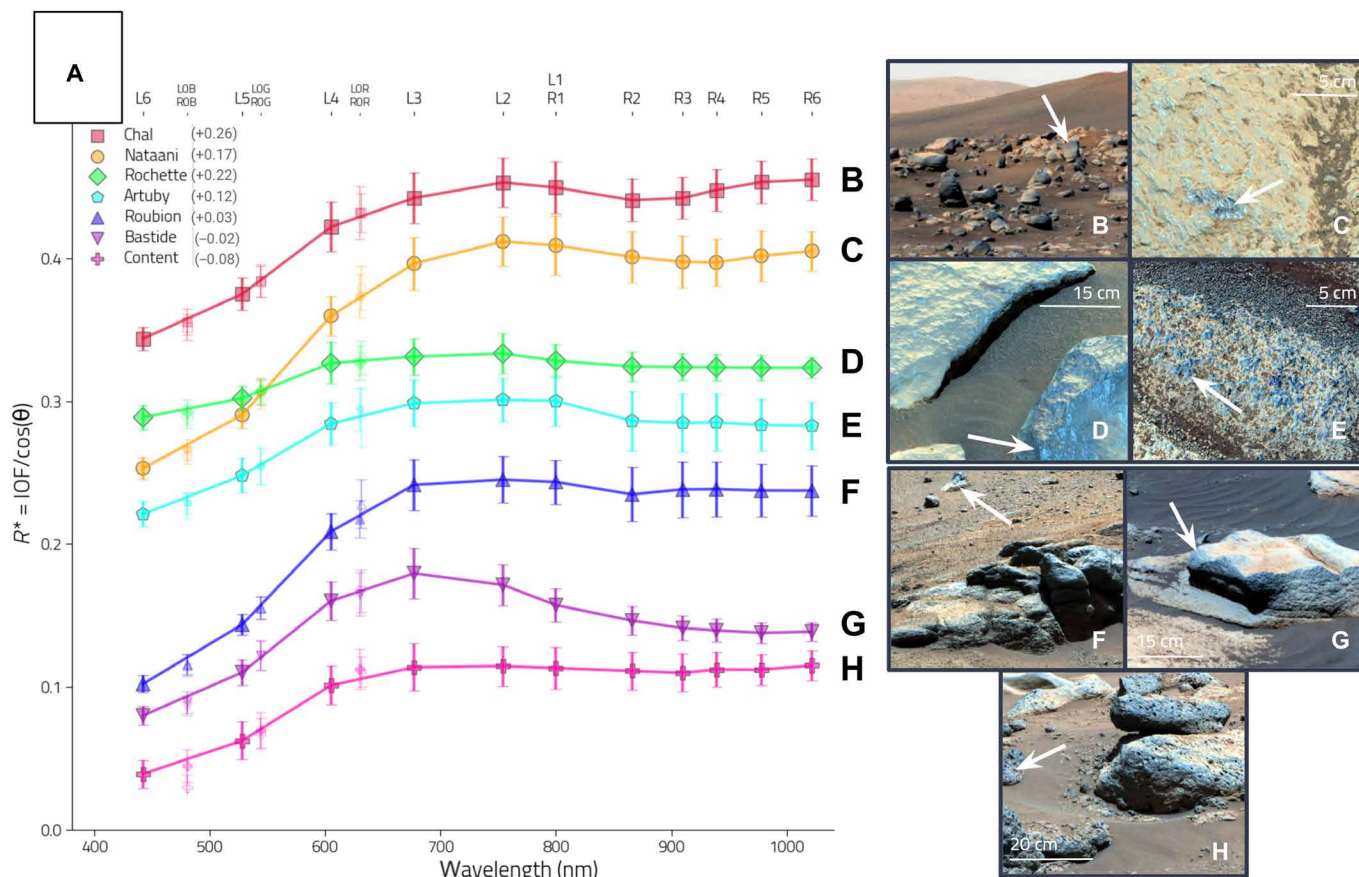
Fig. 8. Representative Mastcam-Z spectra and context images from each stratigraphic member. (**A**) Representative spectra, keyed to the enhanced R0 Bayer filter context images at right. Larger bold plot symbols represent 11-band narrowband filter data, while smaller lighter symbols represent Bayer RGB filter data. White arrows indicate locations from which spectra were extracted. (**B**) Ch'ał (sol 123, zcam03169, image ~2 m across at distance of indicated rock). (**C**) Naat'áanii (sol 80, zcam03129). (**D**) Rochette (sol 193, zcam03217). (**E**) Artuby (sol 138, zcam03181). (**F**) Roubion (sol 175, zcam03205, image ~2 m across at distance of indicated rock). (**G**) Bastide (sol 213, zcam03235). (**H**) Content (sol 247, zcam03249). Error bars represent spatial variance within each region sampled.

the light-toned patches that appear to reflect secondary mineralization filling cavities. The sample cores and associated abraded surfaces from the Séítah formation rocks reveal coarse-grained (~2.0 to 3.0 mm) aggregate textures [fig. S8 (D and G) of the Brac and Issole samples]. The granular nature of Séítah rocks is evident in the more angular, rugged ends of sample cores Salette, Coulettes, Robine, and Malay (fig. S8, E, F, H, and I). The light-toned, greenish mineral grains in the Séítah formation samples are consistent with the Mastcam-Z olivine-bearing spectral interpretation seen in Séítah formation outcrops (Fig. 8). Olivine has also been identified by x-ray fluorescence and Raman mapping obtained on the abrasion surfaces Dourbes and Quartier by the Perseverance PIXL and SHERLOC instruments, consistent with the interpretation of Séítah as an igneous olivine cumulate (*14, 15*). Some amount of brown staining is also evident in the Séítah abrasion and sample core images (fig. S8).

Interpretations. The textures and features observed in outcrops of the Máaz and Séítah formations as observed with the unique combination of spatial resolution and spatial/spectral coverage of Mastcam-Z images are largely consistent with an igneous origin [e.g., (*16*)]. In particular, the structureless textures with curvilinear voids (*9*) show similarities to vesicular lava flows in some locations (e.g., Fig. 6). In other locations such as the rim of Adziilii crater and

the Citadelle outcrop on the Artuby ridge, complex lobe/intraflow textures are reminiscent of low-viscosity pahoehoe flows. Evidence is also seen for flow banding, flow foliation, and vesicular textures (potentially enhanced due to wind erosion) suggestive of gas bubble formation during extrusion (e.g., Fig. 7).

However, impact processes have also clearly modified the surface materials in Jezero, as most obviously evidenced by the numerous craters visible from orbit and down to rover scales (e.g., Fig. 1 and fig. S2). In the field, impactites typically share many characteristics with volcanic rocks, including potential flow patterns and textures like banding or foliation and compositional signatures similar to those of typical basaltic compositions [e.g., (*17*)]. While specific definitive evidence of impact-related genesis or modification has not yet been seen in Jezero floor rocks (e.g., shatter cones in images or confirmed presence of maskelynite or diaplectic glass in abrasion patches investigated by SHERLOC or SuperCam), the potential origin and/or modification of many of these materials by impact processes remains a valid hypothesis to test.

Thus, the natural surface textures and outcrop geometries of the parts of the Máaz and Séítah formations so far observed are not uniquely consistent with a specific origin. Their spectral properties are also not definitively diagnostic, as the strong olivine signatures

in Séítah rocks, as opposed to the pyroxene signatures in Máaz formation and Content member rocks, could be due to either density sorting within a single igneous unit [e.g., (11)] or the emplacement of distinct lava flows. Both formations show signs of variable oxidation that could be related to alteration either during or long after emplacement, as well as surface coatings that postdate wind erosion and likely imply alteration under more modern conditions (fig. S7).

To date, the rocks in the western delta scarp and remnants are the only imaged rocks with an unambiguously sedimentary origin (10). The Perseverance rover has also not thus far encountered obvious primary-deposited tephra (tuff) deposits, impact breccias, or other specific lithologies. However, high-resolution images of some specific rock and outcrop morphologies and textures are potentially consistent with sedimentary or pyroclastic origin hypotheses. For example, the subcentimeter-scale stratification within some outcrops in the Máaz formation at Mure and along the Artuby ridge could be consistent with either volcanic/volcaniclastic or perhaps intra-lava flow fluvial/lacustrine sedimentary deposition (Fig. 6 and fig. S4). However, the stratified outcrops so far encountered on the crater floor do not show evidence of fluvial/lacustrine or pyroclastic density current structures such as cross-bedding, ripples, imbrication, scour and fill structures, or graded bedding (normal or reverse). While the structureless layers of the outcrops encountered at Mure and along the Artuby ridge have features that are most consistent with a lava flow origin, a sedimentary origin is possible for the lower thinly layered parts (Figs. 6 and 7 and fig. S4) or for extensions of these strata that continue into the subsurface as measured by RIMFAX (18). For example, the finer strata could potentially be primary and/or reworked pyroclastic sediments as opposed to fluvial or lacustrine sediments.

The interpretation that many of the Jezero crater Máaz formation rocks and strata thus far encountered are volcanic or volcaniclastic in origin is consistent with some aspects of conclusions derived from other Mars 2020 instruments. Specifically, visible to near-IR reflectance spectra from the SuperCam instrument have been interpreted to reveal an igneous terrain with compositional and possible mineral density stratification (11), consistent with potential local magmatic extrusion and/or eruption. SHERLOC data have been interpreted to suggest that the degree of aqueous alteration of the mafic to ultramafic protolith was relatively low because large olivine-rich domains remain intact within Séítah (14), and PIXL results have been interpreted to be consistent with a cumulate igneous unit within Séítah (15). The geographically related presence of extrusively or explosively emplaced volcanic rocks in the Máaz formation is consistent with the hypothesized presence of intrusive igneous cumulates in the underlying Séítah formation.

Integrated payload results from SuperCam, SHERLOC, and PIXL, along with mineralogic inferences from Mastcam-Z multispectral observations, suggest that alteration materials—including carbonates, hydrated silicates, sulfates, perchlorates, and iron oxides—are pervasive in the Jezero crater floor but low in abundance. Observations of the Máaz and Séítah formations suggest that the presence of an overlying ancient Jezero lake did not cause substantial open-system alteration or leaching of these rocks. This could be because the ancient Jezero lake was short-lived relative to typical chemical weathering time scales during warmer paleoclimate conditions and/or that environmental conditions were prevalently cold. The slow kinetics of basaltic protolith alteration and secondary mineral precipitation at low temperatures could also explain the relatively low abundances

of many alteration phases but still be consistent with the presence of carbonates. Alternatively, the same erosional processes that have worn back and apparently removed many of the ancient delta sediments from the crater could also have substantially deflated the original, more altered rocks on the crater floor. Future exploration of the crater floor as well as of lacustrine and fluvial sediments at the Jezero delta will allow the Perseverance team to test these hypotheses.

Regolith morphologies, textures, and multispectral properties

Observations. Differences in texture, tone, color, and distribution characterize four broad components of the regolith on the Jezero crater floor (Fig. 9). These include coarse, dark-toned, gray grains that occur as well-sorted, aeolian-transported sand (≤1-mm grain sizes) found commonly on megaripple surfaces (Fig. 9, A, B, and D). A second regolith component includes coarser (1 to 2 mm diameter), subrounded gray grains that are not associated with bedforms and occur around the bases of larger rocks, suggestive of a lag deposit (Fig. 9, A and D). These grains are bluer in color than finer-grained regolith materials, with a peak reflectance at 677 nm and flat to negative near-IR slopes consistent with a broad ~1000-nm absorption—a spectral signature consistent with olivine (Fig. 9A), which has also been identified in SuperCam LIBS measurements of coarse-grained regolith (19).

A finer-grained, redder regolith component is mixed with and typically underlies the coarser components. This redder regolith also occurs in depressions on the tops of rocks. Wheel tracks and dislodged rocks resulting from rover activity disturb the uppermost surface, revealing the finer-grained and darker-toned underlying regolith. In places, they also provide evidence of a crust of more indurated regolith at the surface (Fig. 9E). This regolith component has a peak reflectance at 754 nm and a broad absorption centered at 908 nm, consistent with pyroxene and a possible ferric iron component (Fig. 9A). Last, pebble- and cobble-sized rock fragments characterize a regolith component that typically occurs where aeolian bedforms are absent (Fig. 9B).

Interpretations. While the coarsest of the gray grains collect at the bases of some exposures of Máaz formation rocks, spectral differences observed between these grains and nearby rocks suggest that they are not genetically related (Fig. 9B). However, their spectral properties are consistent with the olivine-dominated rocks in the Séítah formation (e.g., Fig. 8) and thus could have formed by weathering, erosion, transport, and preferential accumulation (20) of olivine from Séítah formation outcrops. In general, the provenance of these mobile sand grains is difficult to constrain, and their sources could be quite distant. Spectral similarities to the pyroxene-like spectra of Máaz formation rocks support the hypothesis that such rocks could be a local source for the finer-grained, redder regolith component. Fine-grained regolith likely incorporates some amount of airfall dust as well. Although less dusty than other landing sites, dust is present in various thicknesses across most surface materials (e.g., Fig. 8G). The dust has visible to near-IR spectral properties consistent with fine-grained crystalline or amorphous nanophase ferric oxides, exhibiting stronger absorptions near 530 and 860 nm (Fig. 9A).

Evidence for physical weathering and erosion and formation of coarse-grained regolith via comminution and in situ weathering of specific rocks and outcrops has been observed in Jezero crater rocks [e.g., (9)]. However, that evidence is rare, and aeolian processes have clearly mixed and homogenized the overall distribution of regolith materials. Active aeolian transport of granular materials during strong
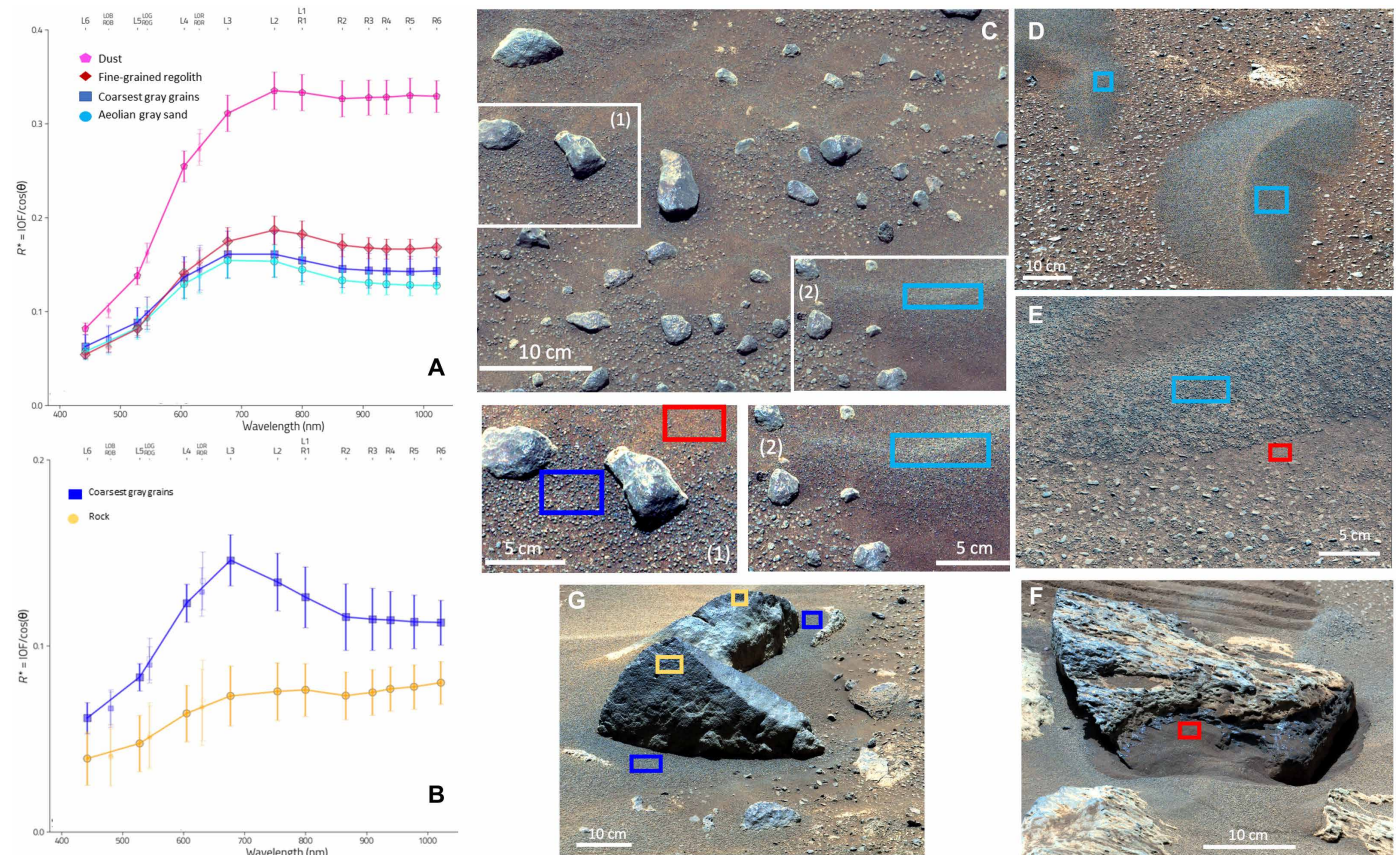
Fig. 9. Examples of distinct Jezero crater regolith textures, morphologies, and spectral properties. (**A**) Spectra from same-colored ROIs in (C) to (F), except for the dust spectrum, which is an average of a large number of relatively uniform "optically thick dust" deposits seen on many rocks in the Máaz and Séítah formations. (**B**) Spectra from same-colored ROIs in (G). (**C**) Examples of three different regolith textural/morphologic types in the same scene: coarse-grained gray and fine-grained red (inset 1) and aeolian gray sand (inset 2). Sol 286, zcam3265. (**D**) Example of a small bedform on top of "mixed" natural regolith surface. Sol 104, zcam03151. (**E**) Example of coarse gray grains, potentially armoring a bedform. Sol 106, zcam03153. (**F**) Example of disturbed soil with wheel track. The rock movement exposes the finer-grained regolith beneath the surface and the apparent surface crust. Sol 130, zcam03175. (**G**) Example of coarse gray grains not spectrally similar to rocks they are near, suggesting that they are sourced elsewhere. Sol 103, zcam03150. Error bars represent spatial variance within each ROI sampled.

wind events has been directly observed several times during the mission thus far [e.g., (21)].

Delta observations and interpretations
While the focus of the rover's first Earth year of exploration was on the Jezero crater floor, high-resolution images acquired during that time and reported here substantially extend the resolution, coverage, and/or quality (illumination conditions) of previously reported Mastcam-Z and SuperCam RMI images of the southeast-facing scarps and erosional remnants of Jezero's western fan deposits (Fig. 5). These observations support the hypothesis that the delta scarp and remnants like the Kodiak butte are the stratigraphically youngest materials in the crater [e.g., (2)]. These images are consistent with classical Gilbert-type deltaic features interpreted as bottomset, foreset, and topset beds (10). The putative bottomsets contain subhorizontal planar stratification of what has been interpreted to have been fine-grained sediments (sand-sized or finer); the foresets likely contain sandstones with pebbles and cobbles, the topsets are subhorizontally stratified, and the uppermost parts of the western fan scarp have been interpreted as a boulder conglomerate (10).

Meteorology and surface-atmosphere interactions
Dust optical depth and particle sizes
Analysis and modeling (see the "Dust characterization and modeling methods" section for details) of multispectral imaging of the Sun, clouds, and sky provide results that directly characterize atmospheric dust and ice aerosols to understand the current climate of Mars and potential hazards for future exploration. Direct solar imaging and near-Sun observations in Jezero have occurred at a much higher intra- and intersol cadence than during previous Mars surface missions, enabling almost daily characterization of column-integrated aerosol abundance and particle size at carefully chosen local solar times and viewing geometries. These results provide quantitative local validation of nearly continuous planet-wide, orbiter-based atmospheric studies over the past 13 Mars years [e.g., (22, 23)].

Perseverance landed in early northern spring at a time of moderate atmospheric dust content and later observed seasonal declines in dust optical depth as well as occasional ice clouds and hazes (Fig. 10A). Over the first 275 sols (solar longitude $L_s \sim 20°$ to 135°,
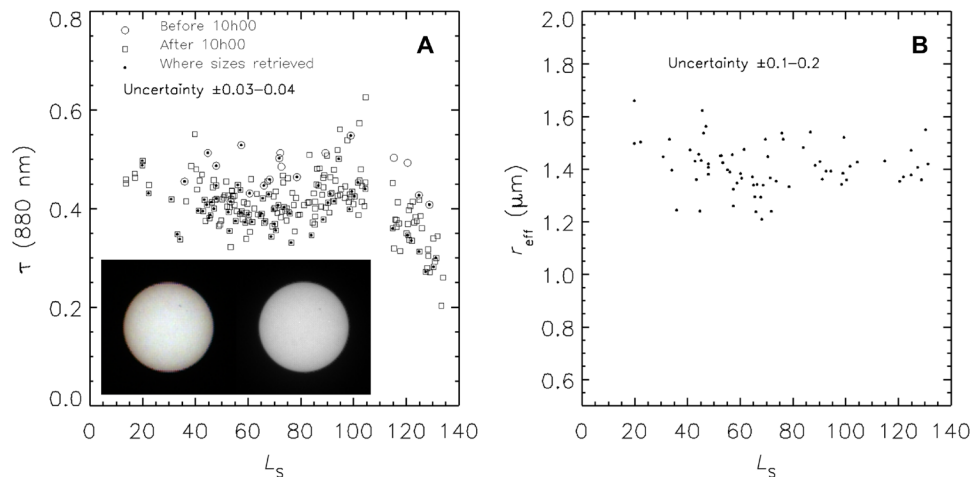
Fig. 10. Dust optical depth and size variations above Jezero crater. (**A**) Derived atmospheric optical depth in Jezero crater based on direct solar imaging observations. Inset shows examples of solar disk (and sunspots) images acquired through ND RGB (left) and 880-nm (right) filters. (**B**) Effective radius of the observed dust aerosols as a function of Mars season (L_S) through sol 274 (27 November 2021).

through about mid-Northern summer), observed 880-nm optical depths of 0.4 to 0.5 were consistent with seasonal expectations for dust [e.g., (24)]. The early summer decline to an optical depth (τ) of ~0.25 mimics trends at other Mars landing sites at the same season [e.g., (24–26)]. The optical depth record will expand to include dust storms that can be studied by the full suite of meteorological instruments, as at previous sites [e.g., (21, 27, 28)]. Solar images also occasionally contain large sunspot groups (Fig. 10A). They contribute no appreciable error to the optical depth inferred from solar flux but instead enable unique monitoring of solar activity on different parts of the Sun than visible from the Earth or from interplanetary heliophysics satellites.

Morning water-ice hazes were present throughout the first 300 sols of the mission. Ice cannot typically be distinguished from dust in the extinction measurements, due to their similar 2- to 4-μm aerosol diameters (29, 30). Ice content is instead inferred from the diurnal behavior—observations before about 10:00 a.m. local time are systematically elevated by Δτ = 0.05 to 0.10 compared to observations in warmer parts of the day (Fig. 10A)—along with prior knowledge of the seasonal presence of water ice around Mars's aphelion [e.g., (29, 31)].

Figure 10B presents the derived column-integrated dust aerosol particle sizes through sol 275, including the observations where some water ice might be present (i.e., before 10:00 a.m.) although the dust optical depth is still anticipated to be the dominant source. The derived particle sizes near 1.4 μm are consistent with previous characterization efforts from other rovers and orbital platforms [see (27)] but provide much higher temporal sampling for correlating locally observed meteorology with synoptic- or global-scale atmospheric behavior.

Despite frequent sky imaging by Mastcam-Z and Navcam (32), discrete ice clouds were rare during the first 300 sols of the mission. Brief exceptions occurred around sols 70 and 170, when clouds were seen in many images, and around sols 250 to 275, when discrete clouds appeared in increasingly clear skies (fig. S9).

Surface-atmosphere interactions

Wind abraded rocks. Multispectral imaging also constrains boundary layer phenomena and surface-atmosphere interactions. A record of long–time scale surface-atmosphere interactions in Jezero (seasonal to billions of years) is being assessed through observations and analysis of oriented flutes, pits, scoops, and gouges in rocks that indicate abrasion by wind-driven sand and the direction of the most energetic winds when abrasion occurred (20, 33–36).

Abundant wind-abraded rocks and aeolian bedforms have been observed at the landing site and along the rover's traverse through sol 180, providing evidence for both recent and ancient prevailing wind directions [e.g., (21)]. We measured the 3D orientations of a variety of flutes, regolith wind tails, and other aeolian features using high-resolution DTMs (see Fig. 4G and Materials and Methods for details on DTM generation from stereo imaging) to infer the orientation of the winds that formed them and compared these azimuths with azimuths determined from examination of MRO/HiRISE and other orbital images, climate model predictions, and wind data acquired by the rover's Mars Environmental Dynamics Analyzer investigation (37). One or two flutes were measured on each of 13 specific rock surface ventifacts in the DTMs, yielding a mean azimuth of 95° ± 7° (implying sand-transporting winds from the west-northwest). However, similar measurements of 16 presumably younger regolith wind tails, indicators of more recent winds, show that present-day sand-driving winds typically blow from the east-southeast (nearly the opposite direction; mean azimuth = 292° ± 17°).

Atmospheric modeling generally predicts net annual sand transport from the east-southeast at present (38), consistent with our Perseverance regolith wind tail results as well as with orbital observations (39). The very different orientation of rock surface aeolian abrasion features at the site supports the hypothesis that they were formed under a different climate regime. Such marked differences in orientations of recent and paleo-wind indicators have been noted at other Mars surface locations [e.g., (36, 40)] and may be a result of major orbital/axial changes that can cause significant changes in atmospheric circulation [e.g., (41)].

Dust lifting and transport during Ingenuity helicopter flights. Six flights of the Ingenuity helicopter (42) have so far been documented using the high spatial resolution and video capabilities of the Mastcam-Z instrument, including each of the first five historic

Table 2. Six video-documented flights of the Ingenuity helicopter.

Flight	Sol	Earth date	Flight time (s)	Description
1	58	19 April 2021	39	Hover to 3 m; rotate body 90°, hover in place (~0-m lateral distance); land near takeoff site. First flight of a powered aircraft on another world
2	61	22 April 2021	52	Hover to 5 m; ±2-m lateral motion; land near takeoff site
3	64	25 April 2021	80	Hover to 5 m; lateral flight to 50 m; return; land near takeoff site
4	69	30 April 2021	117	Hover to 5 m; lateral flight to 133 m; return; land near takeoff site. First recorded sounds of helicopter flight (66)
5	76	7 May 2021	108	Hover to 5 m; lateral flight to 129 m south; hover to 10 m; land at 129-m distance
13	193	5 September 2021	160	Hover to 8 m; lateral flight of 210 m; return to the northeast and back, returned to within ~12 m of takeoff site. First "science scouting" flight, over Séítah ridge

flights (Table 2). Both natural and rotor-induced dust lifting were observed in the images and videos (fig. S10). All flights occurred near local noon when high convective activity was expected. The first five take-offs and four landings all took place in the rover-disturbed area of the original Ingenuity drop-off location. Dust lifting was associated with each event. During flight 4, the helicopter flew out of frame to the south (the camera mast could not "track" the helicopter during flight) and returned into the frame within a large dust cloud moving with the helicopter. Figure S10 (top) shows the flight-4 dust cloud using mean-frame removal to identify changes in the scene and converting to an optical depth overlay based on the contrast changes of the background. The lateral optical depth of the dust cloud was 0.02 to 0.10, where low optical depths could be reliably measured only against shadowed areas. The dust cloud was observed to enter the frame ahead of the helicopter and moved with the helicopter across the frame before a landing out of the frame lifted more dust, moving north or north and west (where west was into the frame). It is clear that some part of the flight had substantial dust raising and that the cloud accumulated and followed the helicopter with the winds, which were from east-southeast at 5 ± 1 m/s at the rover location (21), implying that the dust cloud moved both to the right and away from the rover. The source region has not been identified.

Dust devils. Short–time scale behavior of local sources of dust in the boundary layer has also been investigated in Jezero through imaging of dust devils, thermal vortices that raise and entrain dust (21, 33, 43–46), and the assessment of the rate and properties of dust sedimentation on rover deck-mounted calibration targets. Dust devils have been commonly observed at the site (21) and have appeared in some of the helicopter flight videos, including one >16 m in diameter (fig. S10).

DISCUSSION

Jezero crater was selected as the landing site for the Perseverance rover because evidence from orbital images suggested that it once contained a lake and preserves evidence for a possible delta deposit at the terminus of its western inlet channel. Mastcam-Z and SuperCam long-distance observations provide strong evidence for a Gilbert-type deltaic origin for what have been interpreted to be the stratigraphically highest deposits in the crater (10).

Mastcam-Z images and multispectral data provide novel information on the texture, morphology, and stratigraphy of a wide variety of rocks on the crater floor of Jezero. The morphologic, lithologic, and mineralogic features observed (including evidence for pyroxene, olivine, and crystalline hematite) are consistent with lightly aqueously altered igneous rocks that have experienced local impact disruption of varying degrees, followed by aeolian modification.

Two distinct geologic formations have been characterized from Mastcam-Z data based on morphologic and mineralogical character. The distinctly layered Séítah formation is exposed in an erosional window to the south and west of the landing site (Figs. 1 and 6 and figs. S5 and S6). While the presence of layering in Séítah is potentially consistent with either igneous or sedimentary origins, Mastcam-Z multispectral and morphologic results presented here as well as results from the rest of the integrated Perseverance payload (9, 11, 14, 15) suggest that the Séítah formation represents an igneous olivine cumulate deposit.

In contrast, the overlying Máaz formation displays a variety of macroscopic morphologies ranging from massive lithologies to layered strata. Mastcam-Z–based interpretation of the morphological expression and textures observed on some Máaz outcrops (for example, vesicularity, complex lobe/intraflow patterns, flow banding, and flow foliation), together with mineralogical evidence of their iron-bearing silicate mineralogy being dominated by pyroxene (Figs. 3 and 6 to 8 and fig. S4), indicates primary formation by lava flows. However, an impactite origin cannot be ruled out and the thin centimeter-scale stratification within some of these layers could represent aeolian strata or pyroclastic deposits.

Geochronology of returned igneous or impact rock samples from the crater floor has the potential to provide constraints on the absolute timing and duration of fluvial events in Jezero through stratigraphic relationships with the delta, as well as constraints on the timing and evolution of igneous activity on the crater floor and surroundings and of key events on Mars more generally through calibration of the crater chronology (7, 47).

We have found no compelling evidence for lacustrine sedimentation in the crater floor regions thus far explored using the rover. Any lacustrine sediments in the region explored so far were apparently either buried by igneous or impact processes, eroded away, or a combination of both.

Last, the amount of atmospheric dust aerosol observed above Jezero crater met seasonal expectations, while morning ice hazes were common and afternoon ice clouds were episodically seen. The dust size distribution was consistent with prior observations with a cross-sectional weighted average radius typically near 1.4 µm. The local processes that maintain atmospheric dust were observed and characterized in images and video of dust devils, and vortex-induced dust transport processes were observed at unprecedented high temporal frequency in videos of the Ingenuity helicopter's rotor-induced dust lifting events.

MATERIALS AND METHODS
Instrumentation and calibration
Mastcam-Z comprises a pair of multispectral, 4:1 zoomable, focusable 1648×1214 pixel CCD cameras (1, 48) that are mounted 1.985 m above ground level on Perseverance's remote sensing mast, providing color stereo images and videos of the scene around the rover. As of mission sol 328 (21 January 2022), 2337 imaging sequences had been commanded to acquire and downlink 34,744 unique raw Mastcam-Z images and more than 44,880 raw video frames. At the lowest zoom setting, the cameras have a focal length of 26 mm, a field of view (FOV) of 25.5° × 19.1°, and a pixel scale of ~540 µm at a 2-m distance and ~27 cm at a 1-km distance. At the highest zoom, the focal length is 110 mm, the FOV is 6.2° × 4.2°, and the pixel scale is ~148 µm at 2 m and ~6.7 cm at 1 km. Each camera head carries an eight-position filter wheel that contains an IR-cutoff filter for color imaging through the detector's Bayer-pattern microfilters, a neutral density (ND) solar filter for imaging the Sun, a common filter centered at 800 nm (18-nm full width at half maximum) to accommodate stereo imaging, and five additional narrowband geology filters (1). Together, this filter set allows the acquisition of 11-point narrow-band spectra between 442 and 1022 nm. The ND filters allow solar imaging at Bayer RGB (ND6) and at 880 nm (ND5), respectively. The camera heads are separated by 24.3 cm with a total toe-in angle of 2.3° between the optical boresights, which allows the generation of stereo terrain models with approximate range resolution of ~0.4 mm at 2 m and ~1 m at 1 km (using 110-mm zoom and assuming a 0.25-pixel correlation error; see Materials and Methods for details). Images acquired by Mastcam-Z are converted to radiance (W m^{-2} sr^{-1} nm^{-1}) with an accuracy of ~5% (40).

The Mastcam-Z primary and secondary radiometric calibration targets (49) are mounted on the rear, starboard side of the rover (fig. S11) and are routinely imaged by the cameras. The primary target (mass, 103 g) is a gold-anodized aluminum base carrying a black-painted gnomon, four concentric grayscale, ceramic rings, and eight circular ceramic color and grayscale patches mounted on top of strong hollow-cylinder permanent magnets that repel magnetizable dust from their central surfaces. The secondary target (mass, 15 g) is a simple aluminum L-bracket carrying 14 square, ceramic color and grayscale patches, seven mounted vertically and seven mounted horizontally. The targets are routinely imaged to accompany multispectral image sequences of targets on the surface. Most calibration target images are acquired within a few hours of local noon. The photometric properties of the calibration targets are well understood from preflight testing and in-flight validation, enabling radiance-calibration of images to absolute accuracies of 5 to 10% (48, 49).

The Mastcam-Z radiometric calibration pipeline uses the results of the preflight calibration (48) to convert raw images in units of observed digital number (DN) to average in-band radiance in units of W m^{-2} sr^{-1} nm^{-1}. The pipeline applies corrections for detector bias and response (flat field) and scales images by the appropriate factors to convert DN to radiance as a function of filter and zoom position. For each radiance image, a corresponding error map is produced that combines the propagated one-sigma error for all calibration parameters and photon counting statistics. A pixel identification map is also produced to highlight dead, hot, saturated, and potentially nonlinear pixels.

Once radiance images are produced by the radiometric calibration pipeline, they are then converted to radiance factor (approximate reflectance) values using the closest available image of the calibration target. The radiance factor (also known as incidence-over-reflectance, IOF, or I/F) is defined as the radiance emitted from a surface relative to the radiance that would be emitted by a perfectly Lambertian surface under the same illumination conditions and oriented normally to the incident sunlight. This is also π times the bidirectional reflectance, or π·radiance/irradiance where irradiance is power per time per unit area normal to the incident beam. IOF is a convenient measure because the definition requires no knowledge of the incidence angle of illumination on the surface. If the angle of incidence is known (or assumed), IOF may be converted to reflectance factor or R^* ("r-star") by $R^* = \text{IOF}/\cos(i)$ [e.g., (50)].

The incident irradiance in each filter is found by making a linear fit of observed radiance to the known reflectance of the magnetically protected central spots of the circular color and grayscale patches of the calibration target. As of sol 300, these regions had attracted very little dust so no correction for dust is yet required. The derived irradiance values are then used to convert other images in matching filters from radiance to IOF by division (48, 49). A simple atmospheric transmission model corrects for the difference in time of acquisition between calibration target image and the images being calibrated. In most cases, this correction is small (<1%) because the time difference is small (minutes). For each IOF image, an error map is produced that propagates the error map for the radiance image with the additional uncertainty introduced by the IOF conversion estimated from the linear fit described above.

Standard broadband red, green, and blue (RGB) filter imaging combined with visible to near-IR narrowband imaging has permitted the identification of distinct units and materials at hand lens to regional scales. Spectra in up to 14 specific wavelengths are extracted from multispectral images by selecting regions of interest (ROIs) from which R^* values are averaged. Spectra from the left and right Mastcam-Zs are scaled to their average value at 800 nm (the L1/R1 narrowband, stereo filters), and error bars shown indicate the SD of pixels within each ROI, which is generally much larger than the instrumental uncertainty (48). Multispectral variations can be caused by changes in texture, subpixel-scale surface relief (including grain size), illumination and viewing conditions, or the presence of surface coverings or coatings. They can also be linked to compositional and/or mineralogic properties related to the presence of certain classes of Fe^{2+}-bearing silicates, Fe^{3+}-bearing oxides or oxyhydroxides, and OH- or H$_2$O-bearing alteration minerals (1), although some important and likely abundant phases (e.g., plagioclase) cannot be uniquely identified from imaging in the 400- to 1000-nm region. Multispectral images and mosaics—rendered as approximate true color, decorrelation stretches, principal component stretches, or other band parameters maps—provide a rapid way to assess the properties of newly encountered terrains and targets. Surface integrals of ROIs

across all filters produce spectra upon which quantitative analyses of specific targets can be performed. These data often inform follow-up by other rover instruments with more precise compositional and spectroscopic capabilities.

Most of the instrument parameters used by the radiometric calibration pipeline, including the detector gain and responsivity, dark current, optical throughput (i.e., effective *f*-number), and amplitude of the modulation transfer function (MTF), have been validated by in-flight calibration activities on Mars. Other aspects of the camera calibration, such as sky flat observations to augment flat field correction maps, focus prediction models, and camera model coefficients, have been updated by in-flight calibration activities. A series of zero-second exposure shutter frames were also acquired on Mars to train the shutter frame simulation model [see (*48*)] used to remove static and dynamic bias contribution. All raw images from the Perseverance rover are quickly made publicly available on a NASA website (https://mars.nasa.gov/mars2020/multimedia/raw-images), and all calibrated Mastcam-Z radiance and radiance factor images are routinely being archived for public release via the NASA Planetary Data System's Cartography and Imaging Sciences Node (https://mastcamz.asu.edu/mastcam-z-data-for-all) (*51*).

Stereo image processing and DTM methods and products

The Mastcam-Z stereo camera system uniquely enables detailed measurements of the topography of rocks, outcrops, and other geological features for precise 3D visualization and stratigraphic mapping. The creation of such spatially extensive fine-scale DTMs is not possible either using the relatively small number of monoscopic SuperCam RMI images or using Navigation and Hazard Camera images, which are at too-low spatial resolution to resolve critical textural and/or granular details.

3D vision processing uses standard stereo photogrammetry to perform a sequence of individual processing steps, based on precise knowledge about the instrument's geometric parameters and the known pointing angles of the pan-tilt unit on the remote sensing mast. The individual steps can be summarized as follows:

1) Stereo matching between left and right camera image to gain a dense set of corresponding points.

2) 3D triangulation to generate a 3D mesh for each corresponding point pair, making use of the known stereo geometry.

3) Projection of image texture onto the mesh.

4) Data fusion between adjacent meshes.

5) For the 2D mosaic case: Projection of camera textures onto an infinite virtual cylindrical or spherical gridded model and mosaicking between adjacent patches with optimization criteria to minimize visual effects on the borders between patches.

6) Optimization of 3D data structures to enable the following real-time rendering of huge datasets: Production of an OPC (ordered point cloud).

Using the specialized software PRo3D (short for Planetary Rover 3D Viewer), these 3D products can be viewed, analyzed, and annotated for scientific analyses [e.g., (*52*)]. Possible analyses include but are not necessarily limited to the measurement of scales (figs. S1, S4, and S5), dip and strike (figs. S4 and S5), altitude, areal coverage, slopes, and other geometric relationships that can be directly obtained from a high-resolution OPC. The spatial information uses the Perseverance pose (position and rotation angles), which is provided by the Jet Propulsion Laboratory engineering team for each position change. This allows the application of a 3D Helmert transform of all obtained datasets OPCs, meshes, and mosaics into a Mars-global reference frame for 3D data fusion in a geometrically consistent manner.

Dust characterization and modeling methods

Direct solar imaging at RGB and IR wavelengths [e.g., (*24*)], supplemented by sky imaging, is used to track the aerosol content of the atmosphere above Jezero crater. Extinction measurements via direct solar imaging enable the most accurate method available for measuring column-integrated aerosol optical depth (*24, 53, 54*). When combined with high radiometric fidelity images of clouds (fig. S9) and diffuse sky radiance, aerosol particle sizes and other dynamical and macrophysical properties like single scattering albedo are also derived (*21, 46, 55–57*). In addition to the synoptic measurements of the column-integrated optical depth of aerosols, routine atmospheric observations included a set of near-Sun images used to characterize the aerosol particle size through a sampling of the forward diffraction lobe (*30*).

Dust particle size is determined by a nonlinear least-squares minimization between the sky images and a forward model calculated using a multiple-scattering radiative transfer algorithm. The data are constrained to have scattering angles between 7° and 20°, selecting only the portion of the images most sensitive to particle size (e.g., the diffraction lobe) and avoiding the potential issue of scattered light associated with a bright source just outside of the FOV. The forward model is based on the well-known, robust DISORT package (http://www.rtatmocn.com/disort/) [e.g., (*58, 59*)], accessed through the Python-based front-end library pyRT_DISORT (https://github.com/kconnour/pyRT_DISORT) (*60*). An advantage of pyRT_DISORT is the ease-of-use with the selected optimization library, LMFIT (https://lmfit.github.io/lmfit-py/intro.html) (*61*). By fixing the optical depth using the contemporaneous direct solar observation, the best-fit effective radius is found using a grid of radiative properties (and linear interpolation) constructed using oblate cylinders and refractive indices (*62–64*). These observations enable separate fits for dust and water ice based on the distinctly different shape of the scattering phase function outside of the diffraction lobe. This, in turn, enables higher fidelity calculations of the effects of aerosol particle size on radiative budgets in dynamical calculations of both surface and atmospheric heating rates [e.g., (*65*)], especially when correlated with other relevant meteorological and remote sensing observations from the Perseverance rover [e.g., (*21, 32*)].

REFERENCES AND NOTES

1. J. F. Bell III, J. N. Maki, G. L. Mehall, M. A. Ravine, M. A. Caplinger, Z. J. Bailey, S. Brylow, J. A. Schaffner, K. M. Kinch, M. B. Madsen, A. Winhold, A. Hayes, P. Corlies, M. Barrington, R. Deen, E. Cisneros, E. Jensen, K. Paris, K. Crawford, C. Rojas, L. Mehall, J. Joseph, J. B. Proton, N. Cluff, B. Betts, E. Cloutis, A. Coates, A. Colaprete, K. S. Edgett, B. L. Ehlmann, S. Fagents, J. Grotzinger, C. Tate, C. Hardgrove, K. Herkenhoff, B. Horgan, R. Jaumann, J. R. Johnson, M. Lemmon, G. Paar, M. Caballo-Perucha, S. Gupta, C. Traxler, F. Preusker, M. Rice, M. S. Robinson, N. Schmitz, R. Sullivan, M. J. Wolff, The Mars 2020 Perseverance rover Mast Camera Zoom (Mastcam-Z) multispectral, stereoscopic imaging investigation. *Space Sci. Rev.* **217**, 24 (2021).

2. K. M. Stack, N. R. Williams, F. Calef, V. Z. Sun, K. H. Williford, K. A. Farley, S. Eide, D. Flannery, C. Hughes, S. R. Jacob, L. C. Kah, F. Meyen, A. Molina, C. Quantin-Nataf, M. Rice, P. Russell, E. Scheller, C. H. Seeger, W. J. Abbey, J. B. Adler, H. Amundsen, R. B. Anderson, S. M. Angel, G. Arana, J. Atkins, M. Barrington, T. Berger, R. Borden,

B. Boring, A. Brown, B. L. Carrier, P. Conrad, H. Dypvik, S. A. Fagents, Z. E. Gallegos, B. Garczynski, K. Golder, F. Gomez, Y. Goreva, S. Gupta, S. E. Hamran, T. Hicks, E. D. Hinterman, B. N. Horgan, J. Hurowitz, J. R. Johnson, J. Lasue, R. E. Kronyak, Y. Liu, J. M. Madariaga, N. Mangold, J. McClean, N. Miklusicak, D. Nunes, C. Rojas, K. Runyon, N. Schmitz, N. Scudder, E. Shaver, J. SooHoo, R. Spaulding, E. Stanish, L. K. Tamppari, M. M. Tice, N. Turenne, P. A. Willis, R. A. Yingst, Photogeologic map of the Perseverance rover field site in Jezero crater constructed by the Mars 2020 Science Team. *Space Sci. Rev.* **216**, 127 (2020).

3. C. I. Fassett, J. W. Head III, Fluvial sedimentary deposits on Mars: Ancient deltas in a crater lake in the Nili Fossae region. *Geophys. Res. Lett.* **32**, L14201 (2003).

4. S. C. Schon, J. W. Head, C. I. Fassett, An overfilled lacustrine system and progradational delta in Jezero crater, Mars: Implications for Noachian climate. *Planet. Space Sci.* **67**, 28–45 (2012).

5. T. A. Goudge, J. F. Mustard, J. W. Head, C. I. Fassett, S. M. Wiseman, Assessing the mineralogy of the watershed and fan deposits of the Jezero crater paleolake system, Mars. *J. Geophys. Res.* **120**, 775–808 (2015).

6. S. Holm-Alwmark, K. M. Kinch, M. D. Hansen, S. Shahrzad, K. Svennevig, W. J. Abbey, Stratigraphic relationships in Jezero crater, Mars: Constraints on the timing of fluvial-lacustrine activity from orbital observations. *J. Geophys. Res. Planets* **126**, e2021JE006840 (2021).

7. S. Shahrzad, K. M. Kinch, T. A. Goudge, C. I. Fassett, D. H. Needham, C. Quantin-Nataf, C. P. Knudsen, Crater statistics on the dark-toned, mafic floor unit in Jezero crater, Mars. *Geophys. Res. Lett.* **46**, 2408–2416 (2019).

8. B. H. Horgan, R. B. Anderson, G. Dromart, E. S. Amador, M. S. Rice, The mineral diversity of Jezero crater: Evidence for possible lacustrine carbonates on Mars. *Icarus* **339**, 113526 (2020).

9. K. A. Farley, K. M. Stack, D. L. Shuster, B. H. N. Horgan, J. A. Hurowitz, J. D. Tarnas, J. I. Simon, V. Z. Sun, E. L. Scheller, K. R. Moore, S. M. McLennan, P. M. Vasconcelos, R. C. Wiens, A. H. Treiman, L. E. Mayhew, O. Beyssac, T. V. Kizovski, N. J. Tosca, J. A. Hurowitz, K. H. Williford, L. S. Crumpler, L. W. Beegle, J. F. Bell III, B. L. Ehlmann, Y. Liu, J. N. Maki, M. E. Schmidt, A. C. Allwood, H. E. F. Amundsen, R. Bhartia, T. Bosak, A. J. Brown, B. C. Clark, A. Cousin, O. Forni, T. S. J. Gabriel, Y. Goreva, S. Gupta, S.-E. Hamran, C. D. K. Herd, K. Hickman-Lewis, J. R. Johnson, L. C. Kah, P. B. Kelemen, K. B. Kinch, L. Mandon, N. Mangold, C. Quantin-Nataf, M. S. Rice, P. S. Russell, S. Sharma, S. Siljeström, A. Steele, R. Sullivan, M. Wadhwa, B. P. Weiss, A. J. Williams, B. V. Wogsland, P. A. Willis, T. A. Acosta-Maeda, P. Beck, K. Benzerara, S. Bernard, A. S. Burton, E. L. Cardarelli, B. Chide, E. Clavé, E. A. Cloutis, B. A. Cohen, A. D. Czaja, V. Debaille, E. Dehouck, A. G. Fairén, D. T. Flannery, S. Z. Fleron, T. Fouchet, J. Frydenvang, B. J. Garczynski, E. F. Gibbons, E. M. Hausrath, A. G. Hayes, J. Henneke, J. L. Jørgensen, E. M. Kelly, J. Lasue, S. Le Mouélic, J. M. Madariaga, S. Maurice, M. Merusi, P.-Y. Meslin, S. M. Milkovich, C. C. Million, R. C. Moeller, J. I. Núñez, A. M. Ollila, G. Paar, D. A. Paige, D. A. K. Pedersen, P. Pilleri, C. Pilorget, P. C. Pinet, J. W. Rice Jr., C. Royer, V. Sautter, M. Schulte, M. A. Sephton, S. K. Sharma, S. F. Sholes, N. Spanovich, M. St. Clair, C. D. Tate, C. D. Tate, C. D. Tate, C. Ucker, S. J. VanBommel, A. G. Yanchilina, M.-P. Zorzano, Aqueously altered igneous rocks on the floor of Jezero crater, Mars. *Science* **377**, eabo2196 (2022).

10. N. Mangold, S. Gupta, O. Gasnault, G. Dromart, J. D. Tarnas, S. F. Sholes, B. Horgan, C. Quantin-Nataf, A. J. Brown, S. Le Mouélic, R. A. Yingst, J. F. Bell III, O. Beyssac, T. Bosak, F. Calef III, B. L. Ehlmann, K. A. Farley, J. P. Grotzinger, K. Hickman-Lewis, S. Holm-Alwmark, L. C. Kah, J. Martinez-Frias, S. M. McLennan, S. Maurice, J. I. Nuñez, A. M. Ollila, P. Pilleri, J. W. Rice Jr., M. Rice, J. I. Simon, D. L. Shuster, K. M. Stack, V. Z. Sun, A. H. Treiman, B. P. Weiss, R. C. Wiens, A. J. Williams, N. R. Williams, K. H. Williford, Evidence for a delta-lake system and ancient flood deposits at Jezero crater, Mars, from the Perseverance rover. *Science* **374**, eabl4051 (2021).

11. R. C. Wiens, A. Udry, O. Beyssac, C. Quantin-Nataf, N. Mangold, A. Cousin, L. Mandon, T. Bosak, O. Forni, S. McLennan, V. Sautter, A. Brown, K. Benzerara, J. R. Johnson, L. Mayhew, S. Maurice, R. B. Anderson, S. M. Clegg, L. Crumpler, T. S. J. Gabriel, P. Gasda, J. Hall, B. Horgan, L. Kah, C. Legett IV, J. M. Madariaga, P. Y. Meslin, A. M. Ollila, F. Poulet, S. K. Sharma, S. Siljeström, J. I. Simon, T. Acosta-Mayeda, C. Alverez-Llamas, S. M. Angel, G. Arana, P. Beck, S. Bernard, T. Bertrand, T. Bousquet, K. Castro, B. Chide, E. Clavé, E. Cloutis, S. Connell, E. Dehouck, G. Dromart, W. Fischer, T. Fouchet, R. Francis, J. Frydenvang, O. Gasnault, E. Gibbons, L. Hausrath, X. Jacob, H. Kalucha, E. Kelly, E. Knutsen, N. Lanza, J. Laserna, J. Lasue, S. Le Mouelic, G. L. Reyes, R. Lorenz, J. A. Manrique, J. Martinez-Frias, N. Melikechi, T. McConnochie, D. Mimoun, F. Montmessin, J. Moros, N. Murdoch, P. Pilleri, C. Pilorget, P. Pinet, W. Rapin, C. Royer, F. Rull, S. Schroeder, A. Stott, J. Tarnas, N. Turenne, M. Veneranda, D. Vogt, P. Willis, K. M. Stack, K. H. Williford, K. A. Farley; and the SuperCam Team, Compositionally and density stratified igneous terrain in Jezero crater, Mars. *Sci. Adv.* **8**, eabo3399 (2022).

12. E. Ravanis, S. Fagents, C. Newman, B. Horgan, S. Holm-Alwmark, A. J. Brown, J. W. Rice, L. Mandon, M. P. Zorzano, The potential for pyroclastic deposits in the Jezero crater region of Mars from ash dispersal modeling, in *53rd Lunar and Planetary Science Conference*, LPI Contrib. 2678, abstract #1692 (2022).

13. V. Z. Sun, K. M. Stack, Geologic map of Jezero crater and the Nili Planum region, Mars. U.S. Geological Survey Scientific Investigations Map 3464, pamphlet 14 p., 1 sheet, scale 1:75,000 (2020); https://doi.org/10.3133/sim3464.

14. E. L. Scheller, J. R. Hollis, E. L. Cardarelli, A. Steele, L. W. Beegle, R. Bhartia, P. Conrad, K. Uckert, S. Sharma, B. L. Ehlmann, W. J. Abbey, S. A. Asher, K. C. Benison, E. L. Berger, O. Beyssac, O. Bleefeld, T. Bosak, A. J. Brown, A. S. Burton, S. V. Bykov, E. Cloutis, A. G. Fairén, L. DeFlores, K. A. Farley, D. M. Fey, T. Fornaro, A. C. Fox, M. Fries, K. Hickman-Lewis, W. F. Hug, J. E. Huggett, S. Imbeah, R. S. Jakubek, L. C. Kah, P. Kelemen, M. R. Kennedy, T. Kizovski, C. Lee, Y. Liu, L. Mandon, F. M. McCubbin, K. R. Moore, B. E. Nixon, J. I. Núñez, C. R. Sanchez-Vahamonde, R. D. Roppel, M. Schulte, M. A. Sephton, S. K. Sharma, S. Siljeström, S. Shkolyar, D. L. Shuster, J. I. Simon, R. J. Smith, K. M. Stack, K. Steadman, B. P. Weiss, A. Werynski, A. J. Williams, R. C. Wiens, K. H. Williford, K. Winchell, B. Wogsland, A. Yanchilina, R. Yingling, M.-P. Zorzano, Aqueous alteration processes and implications for organic geochemistry in Jezero crater, Mars. *Sci. Adv.* **377**, eabo2196 (2022).

15. Y. Liu, M.M. Tice, M. E. Schmidt, A. H. Treiman, T. V. Kizovski, J.A. Hurowitz, A. C. Allwood, J. Henneke, D. A. K. Pedersen, S. J. VanBommel, M. W. M. Jones, A. L. Knight, B. J. Orenstein, B. C. Clark, W. T. Elam, C. M. Heirwegh, T. Barber, L. W. Beegle, K. Benzerara, S. Bernard, O. Beyssac, T. Bosak, A. J. Brown, E. L. Cardarelli, D. C. Catling, J. R. Christian, E. A. Cloutis, B. A. Cohen, S. Davidoff, A. G. Fairén, K. A. Farley, D. O. Flannery, A. Galvin, J. P. Grotzinger, S. Gupta, J. Hall, C. D. K. Herd, K. Hickman-Lewis, R. P. Hodyss, B. H. N. Horgan, J. R. Johnson, J. L. Jørgensen, L. C. Kah, J. N. Maki, L. Mandon, N. Mangold, F. M. McCubbin, S. M. McLennan, K. Moore, M. Nachon, P. Nemere, L. D. Nothdurft, J. I. Núñez, L. O'Neil, C. M. Quantin-Nataf, V. Sautter, D. L. Shuster, K. L. Siebach, J. I. Simon, K. P. Sinclair, K. M. Stack, A. Steele, J. D. Tarnas, N. J. Tosca, K. Uckert, A. Udry, L. A. Wade, B. P. Weiss, R. C. Wiens, K. H. Williford, M. Zorzano, A ferroan olivine cumulate on the floor of Jezero crater, Mars. *Science* **377**, 1513–1519.

16. R. A. F. Cas, J. V. Wright, *Volcanic Successions: Modern and Ancient* (Chapman and Hall, 1987), 528 pp.

17. G. R. Osinski, E. Pierazzo, Impact cratering: Processes and products, in *Impact Cratering: Processes and Products*, G.R. Osinski, E. Pierazzo, Eds. (Blackwell Publishing, 2013), pp. 1–20.

18. S.-E. Hamran, D. A. Paige, A. Allwood, H. E. F. Amundsen, T. Berger, S. Brovoll, L. Carter, T. Casademont, L. Damsgård, H. Dypvik, S. Eide, A. G. Fairén, R. Ghent, J. Kohler, M. T. Mellon, D. C. Nunes, D. Plettemeier, P. Russell, M. Siegler, M. J. Øyan, Ground penetrating radar observations of subsurface structures in the floor of Jezero crater, Mars. *Sci. Adv.* **8**, eabp8564 (2022).

19. O. Beyssac, O. Gasnault, B. Chide, E. Clave, A. Cousin, O. Forni, C. Royer, J. R. Johnson, K. Benzerara, S. M. Clegg, P. Meslin, P. Pilleri, P. A. Willis, J. Lasue, L. Mandon, A. Ollila, P. Beck, P. B. Kelemen, E. Dehouck, R. B. Anderson, S. Schröder, A. Udry, T. S. J. Gabriel, T. Bosak, N. Turenne, S. Connell, M. Zorzano, C. Quantin-Nataf, A. J. Brown, J. Manrique, T. Fouchet, V. Sautter, S. Le Mouelic, S. K. Sharma, E.Cloutis, P. C. Pinet, S. Maurice, R. C. Wiens, Mafic chemistry and mineralogy (including olivine) of the coarse-grained regolith analyzed by SuperCam at Jezero crater, Mars, paper presented at the Annual Meeting of the American Geophysical Union, New Orleans, LA, 14 December 2021.

20. R. Sullivan, R. Arvidson, J. F. Bell III, R. Gellert, M. Golombek, R. Greeley, K. Herkenhoff, J. Johnson, S. Thompson, P. Whelley, J. Wray, Wind-driven particle mobility on Mars: Insights from MER observations at "El Dorado" and surroundings at Gusev crater. *J. Geophys. Res.* **113**, E06S07 (2008).

21. C. E. Newman, R. Hueso, M. T. Lemmon, A. Munguira, Á. Vicente-Retortillo, V. Apestigue, G. M. Martínez, D. Toledo-Carrasco, R. Sullivan, K. Herkenhoff, M. de la Torre-Juarez, M. I. Richardson, A. Stott, N. Murdoch, A. Sanchez-Lavega, M. Wolff, I. Arruego-Rodriguez, E. S. Martinez, S. Navarro, J. Gómez-Elvira, L. Tamppari, D. Viúdez-Moreiras, A. Hari, M. Genzer, M. Hieta, R. D. Lorenz, P. Conrad, F. Gómez, T. McConnochie, D. Mimoun, C. Tate, T. Bertrand, J. Bell III, J. Maki, J. A. Rodriguez Manfredi, R. Wiens, B. Chide, S. Maurice, M. Zorzano, L. Mora, M. Baker, D. Banfield, J. Pla-Garcia, O. Beyssac, A. Brown, B. Clark, A. Lepinette, F. Montmessin, E. Fischer, P. Patel, T. del Río-Gaztelurrutia, T. Fouchet, R. Francis, S. Guzewich, The dynamic atmospheric and aeolian environment of Jezero crater, Mars. *Sci. Adv.* **8**, eabn3783 (2022).

22. G. M. Martínez, C. Newman, A. De Vicente-Retortillo, E. Fischer, N. Renno, M. Richardson, A. G. Fairén, M. Genzer, S. D. Guzewich, R. M. Haberle, A. M. Harri, O. Kemppinen, M. Lemmon, M. D. Smith, M. Torre-Juárez, A. Vasavada, The modern near-surface Martian climate: A review of in-situ meteorological data from Viking to Curiosity. *Space Sci. Rev.* **212**, 295–338 (2017).

23. W. Sheehan, J. F. Bell III, *Discovering Mars: A History of Observation and Exploration of the Red Planet* (University of Arizona Press, 2021), pp. 581–598.

24. M. T. Lemmon, M. J. Wolff, J. F. Bell III, M. D. Smith, B. A. Cantor, P. H. Smith, Dust aerosol, clouds, and the atmospheric optical depth record over 5 Mars years of the Mars Exploration rover mission. *Icarus* **251**, 96–111 (2015).

25. D. S. Colburn, J. B. Pollack, R. M. Haberle, Diurnal variations in optical depth at Mars. *Icarus* **79**, 159–189 (1989).

26. A. R. Vasavada, S. Piqueux, K. W. Lewis, M. T. Lemmon, M. D. Smith, Thermophysical properties along Curiosity's traverse in Gale crater, Mars, derived from the REMS ground temperature sensor. *Icarus* **284**, 372–386 (2017).

27. D. Viúdez-Moreiras, C. E. Newman, M. de la Torre, G. Martínez, S. Guzewich, M. Lemmon, J. Pla-García, M. D. Smith, A.-M. Harri, M. Genzer, A. Vicente-Retortillo, A. Lepinette, J. A. Rodriguez-Manfredi, A. R. Vasavada, J. Gómez-Elvira, Effects of the MY34/2018 global dust storm as measured by MSL REMS in gale crater. *J. Geophys. Res.* **124**, 1899–1912 (2019).

28. D. Viúdez-Moreiras, C. E. Newman, F. Forget, M. Lemmon, D. Banfield, A. Spiga, A. Lepinette, J. A. Rogriguez-Manfredi, J. Gomex-Elvira, J. Pla-Garcia, N. Muller, M. Grott; and the TWINS/InSight team, Effects of a large dust storm in the near-surface atmosphere as measured by insight in Elysium Planitia, Mars. *J. Geophys. Res.* **125**, e2020JE006493 (2020).

29. R. T. Clancy, M. J. Wolff, P. R. Christensen, Mars aerosol studies with the MGS TES emission phase function observations: Optical depths, particle sizes, and ice cloud types versus latitude and solar longitude. *J. Geophys. Res. Planet* **108**, 2.1–2.20 (2003).

30. M. T. Lemmon, S. D. Guzewich, T. McConnochie, A. de Vicente-Retortillo, G. Martínez, M. D. Smith, J. F. Bell III, D. Wellington, S. Jacob, Large dust aerosol sizes seen during the 2018 Martian global dust event by the *Curiosity* rover. *Geophys. Res. Lett.* **46**, 9448–9456 (2019).

31. M. J. Wolff, J. F. Bell III, P. B. James, R. T. Clancy, S. W. Lee, Hubble space telescope observations of the martian aphelion cloud belt prior to the pathfinder mission: Seasonal and interannual variations. *J. Geophys. Res.* **104**, 9027–9041 (1999).

32. J. N. Maki, D. Gruel, C. McKinney, M. A. Ravine, M. Morales, D. Lee, R. Willson, D. Copley-Woods, M. Valvo, T. Goodsall, J. McGuire, R. G. Sellar, J. A. Schaffner, M. A. Caplinger, J. M. Shamah, A. E. Johnson, H. Ansari, K. Singh, T. Litwin, R. Deen, A. Culver, N. Ruoff, D. Petrizzo, D. Kessler, C. Basset, T. Estlin, F. Alibay, A. Nelessen, S. Algermissen, The Mars 2020 engineering cameras and microphone on the Perseverance rover: A next-generation imaging system for Mars exploration. *Space Sci. Rev.* **216**, 137 (2020).

33. R. Greeley, R. E. Arvidson, P. W. Barlett, D. Blaney, N. A. Cabrol, P. R. Christensen, R. L. Fergason, M. P. Golombek, G. A. Landis, M. T. Lemmon, S. M. McLennan, J. N. Maki, T. Michaels, J. E. Moersch, L. D. V. Neakrase, S. C. R. Rafkin, L. Richter, S. W. Squyres, P. A. De Souza Jr., R. J. Sullivan, S. D. Thompson, P. L. Whelley, Gusev crater: Wind-related features and processes observed by the Mars exploration rover spirit. *J. Geophys. Res.* **111**, E02S09 (2006).

34. R. P. Sharp, Wind-driven sand in Coachella Valley, California. *Geol. Soc. Am. Bull.* **75**, 785–804 (1964).

35. N. T. Bridges, R. Greeley, A. F. C. Haldemann, K. E. Herkenhoff, M. Kraft, T. J. Parker, A. W. Ward, Ventifacts at the Pathfinder landing site. *J. Geophys. Res.* **104**, 8595–8615 (1999).

36. J. E. Laity, N. T. Bridges, Ventifacts on Earth and Mars: Analytical, field, and laboratory studies supporting sand abrasion and windward feature development. *Geomorphology* **105**, 202–217 (2009).

37. J. A. Rodriguez-Manfredi, M. de la Torre Juárez, A. Alonso, V. Apéstigue, I. Arruego, T. Atienza, D. Banfield, J. Boland, M. A. Carrera, L. Castañer, J. Ceballos, H. Chen-Chen, A. Cobos, P. G. Conrad, E. Cordoba, T. Del Río-Gaztelurrutia, A. de Vicente-Retortillo, M. Domínguez-Pumar, S. Espejo, A. G. Fairen, A. Fernández-Palma, R. Ferrándiz, F. Ferri, E. Fischer, A. García-Manchado, M. García-Villadangos, M. Genzer, S. Giménez, J. Gómez-Elvira, F. Gómez, S. D. Guzewich, A.-M. Harri, C. D. Hernández, M. Hieta, R. Hueso, I. Jaakonaho, J. J. Jiménez, V. Jiménez, A. Larman, R. Leiter, A. Lepinette, M. T. Lemmon, G. López, S. N. Madsen, T. Mäkinen, M. Marín, J. Martín-Soler, G. Martínez, A. Molina, L. Mora-Sotomayor, J. F. Moreno-Álvarez, S. Navarro, C. E. Newman, C. Ortega, M. C. Parrondo, V. Peinado, A. Peña, I. Pérez-Grande, S. Pérez-Hoyos, J. Pla-García, J. Polkko, J. Romeral, C. Romero, K. D. Runyon, A. Saiz-Lopez, A. Sánchez-Lavega, I. Sard, J. T. Schofield, E. Sebastian, M. D. Smith, R. J. Sullivan, L. K. Tamppari, A. D. Thompson, D. Toledo, F. Torrero, J. Torres, R. Urquí, T. Velasco, D. Viúdez-Moreiras, S. Zurita; MEDA team, The Mars environmental dynamics analyzer, MEDA. A suite of environmental sensors for the Mars 2020 mission. *Space Sci. Rev.* **217**, 48 (2021).

38. C. E. Newman, M. de la Torre Juárez, J. Pla-García, R. J. Wilson, S. R. Lewis, L. Neary, M. A. Kahre, F. Forget, A. Spiga, M. I. Richardson, F. Daerden, T. Bertrand, D. Viúdez-Moreiras, R. Sullivan, A. Sánchez-Lavega, B. Chide, J. A. Rodríguez-Manfredi, Multi-model meteorological and aeolian predictions for Mars 2020 and the Jezero crater region. *Space Sci. Rev.* **217**, 20 (2021).

39. M. Day, T. Dorn, Wind in Jezero crater, Mars. *Geophys. Res. Lett.* **46**, 3099–3107 (2019).

40. A. G. Hayes, J. P. Grotzinger, L. A. Edgar, S. W. Squyres, W. A. Watters, J. Sohl-Dickstein, Reconstruction of eolian bed forms and paleocurrents from cross-bedded strata at Victoria Crater, Meridiani Planum, Mars. *J. Geophys. Res.* **116**, E00F21 (2011).

41. L. K. Fenton, H. C. Carson, T. I. Michaels, Climate forcing of ripple migration and crest alignment in the last 400 kyr in Meridiani Planum, Mars. *J. Geophy. Res.* **123**, 849–863 (2018).

42. J. Baralam, M. Aung, M. P. Golombek, The Ingenuity helicopter on the Perseverance rover. *Space Sci. Rev.* **217**, 56 (2021).

43. S. M. Metzger, J. R. Johnson, J. R. Carr, T. J. Parker, M. Lemmon, Dust devil vortices seen by the Mars Pathfinder camera. *Geophys. Res. Lett.* **26**, 2781–2784 (1999).

44. F. Ferri, P. H. Smith, M. T. Lemmon, N. Renno, Dust devils as observed by Mars Pathfinder. *J. Geophys. Res.* **108**, 5133 (2003).

45. R. Greeley, D. Waller, N. Cabrol, G. Landis, M. T. Lemmon, L. Neakrase, M. P. Hoffer, S. Thompson, P. Whelley, Gusev crater, Mars: Observations of three dust devil seasons. *J. Geophys. Res.* **115**, E00F02 (2010).

46. M. D. Ellehoj, H. P. Gunnlaugsson, K. M. Bean, B. A. Cantor, L. Drube, D. Fisher, B. T. Gheynani, A.-M. Harri, C. Holstein-Rathlou, H. Kahanpää, M. T. Lemmon, M. B. Madsen, M. C. Malin, J. Polkko, P. Smith, L. K. Tamppari, P. A. Taylor, W. Weng, J. Whiteway, Convective vortices and dust devils at the Phoenix Mars Mission landing site. *J. Geophys. Res.* **115**, E00E16 (2010).

47. S. C. Werner, In situ calibration of the Martian cratering chronology. *Meteorit. Planet. Sci.* **54**, 1182–1193 (2019).

48. A. G. Hayes, P. Corlies, C. Tate, J. F. Bell III, J. N. Maki, M. Caplinger, K. M. Kinch, K. Herkenhoff, B. Horgan, J. Johnson, G. Parr, M. S. Rice, E. Jensen, T. M. Kubacki, E. Cloutis, B. Ehlmann, E. Lakdawalla, R. Sullivan, A. Winhold, M. Barrington, A. Parkinson, J. van Beek, P. Caballo-Perucha, E. Cisneros, D. Dixon, C. Donaldson, O. B. Jensen, J. Kuik, K. Lapo, A. Magee, Pre-flight calibration of the Mars 2020 rover Mastcam Zoom (Mastcam-Z) multispectral, stereoscopic imager. *Space Sci. Rev.* **217**, 29 (2021).

49. K. M. Kinch, M. B. Madsen, J. F. Bell III, J. N. Maki, Z. Bailey, A. G. Hayes, O. B. Jensen, M. Merusi, M. H. Bernth, A. N. Sørensen, M. Hilverda, E. Cloutis, D. Applin, E. Mateo-Marti, J. A. Manrique, G. Lopez-Reyes, A. Bello-Arufe, B. Ehlmann, J. Buz, A. Pommerol, N. Thomas, L. Affolter, K. Herkenhoff, J. R. Johnson, M. Rice, P. Corlies, C. Tate, M. Caplinger, E. Jensen, T. Kubacki, E. Cisneros, K. Paris, A. Winhold, D. Wellington, Radiometric calibration targets for the Mastcam-Z camera on the Mars 2020 rover mission. *Space Sci. Rev.* **216**, 141 (2020).

50. R. J. Reid, P. H. Smith, M. Lemmon, R. Tanner, M. Burkland, E. Wegryn, J. Weinberg, R. Marcialis, D. T. Britt, N. Thomas, R. Kramm, A. Dummel, D. Crowe, B. J. Bos, J. F. Bell III, P. Rueffer, F. Gliem, J. R. Johnson, J. N. Maki, K. E. Herkenhoff, R. B. Singer, Imager for Mars Pathfinder (IMP) image calibration. *J. Geophys. Res.* **104**, 8907–8925 (1999).

51. J. F. Bell, J. N. Maki, Mars 2020 Mast Camera Zoom Data Bundle, from Operations Team, calibrated products. NASA Planetary Data System, doi:10.17189/BS6B-4782 (2021).

52. R. Barnes, S. Gupta, C. Traxler, T. Ortner, A. Bauer, G. Hesina, G. Paar, B. Huber, K. Juhart, L. Fritz, B. Nauschnegg, J. P. Muller, Y. Tao, Geological analysis of Martian rover-derived digital outcrop models using the 3D visualization tool, Planetary Robotics 3D Viewer— Pro3D. *Earth Space Sci.* **5**, 285–307 (2018).

53. P. H. Smith, M. T. Lemmon, Opacity of the Martian atmosphere measured by the Imager for Mars Pathfinder. *J. Geophys. Res.* **104**, 8975–8985 (1999).

54. M. T. Lemmon, M. J. Wolff, M. D. Smith, R. T. Clancy, D. Banfield, G. A. Landis, A. Ghosh, P. H. Smith, N. Spanovich, B. Whitney, P. Whelley, R. Greeley, S. Thompson, J. F. Bell III, S. W. Squyres, Atmospheric imaging results from the Mars Exploration rovers: Spirit and Opportunity. *Science* **306**, 1753–1756 (2004).

55. J. B. Pollack, M. E. Ockert-Bell, M. K. Shepard, Viking Lander image analysis of Martian atmospheric dust. *J. Geophys. Res.* **100**, 5235–5250 (1999).

56. M. G. Tomasko, L. R. Doose, M. T. Lemmon, P. H. Smith, E. Wegryn, Properties of dust in the Martian atmosphere from the Imager on Mars Pathfinder. *J. Geophys. Res.* **104**, 8987–9007 (1999).

57. J. E. Moores, M. T. Lemmon, P. H. Smith, L. Komguem, J. A. Whiteway, Atmospheric dynamics at the Phoenix landing site as seen by the Surface Stereo Imager (SSI). *J. Geophys. Res.* **115**, E00E08 (2010).

58. K. Stamnes, S. C. Tsay, W. J. Wiscombe, K. Jayaweera, Numerically stable algorithm for discrete-ordinate-method radiative transfer in multiple scattering and emitting layered media. *Appl. Optics* **27**, 2502–2509 (1988).

59. I. Laszlo, K. Stamnes, W. J. Wiscombe, S. C. Tsay, The discrete ordinate algorithm, DISORT for radiative transfer, in *Light Scattering Reviews, Volume 11: Light Scattering and Radiative Transfer*, A. Kokhanovsky, Ed. (Springer, 2016), pp. 3–65.

60. K. Connour, M. J. Wolff, N. M. Schneider, J. Deighan, F. Lefèvre, S. K. Jain, Another one derives the dust: Ultraviolet dust aerosol properties retrieved from MAVEN/IUVS data. *Icarus* **387**, 10.1016/j.icarus.2022.115177 (2022).

61. M. Newville, T. Stensitzki, D. B. Allen, A. Ingargiola, LMFIT: Non-Linear Least-Square Minimization and Curve-Fitting for Python. Zenodo 10.5281/zenodo.11813 (2014).

62. M. J. Wolff, M. D. Smith, R. T. Clancy, R. Arvidson, M. Kahre, F. Seelos, S. Murchie, H. Savijärvi, Wavelength dependence of dust aerosol single scattering albedo as observed by the compact reconnaissance imaging spectrometer. *J. Geophys. Res. Planets* **114**, E00D04 (2009).

63. M. J. Wolff, R. Todd Clancy, J. D. Goguen, M. C. Malin, B. A. Cantor, Ultraviolet dust aerosol properties as observed by MARCI. *Icarus* **208**, 143–155 (2010).

64. M. J. Wolff, R. T. Clancy, M. A. Kahre, R. M. Haberle, F. Forget, B. A. Cantor, M. C. Malin, Mapping water ice clouds on Mars with MRO/MARCI. *Icarus* **332**, 24–49 (2019).

65. M. J. Wolff, M. Lopéz-Valverde, J.-B. Madeleine, R. J. Wilson, M. D. Smith, T. Fouchet, G. T. Delory, Radiative process: Techniques and applications, in *The Atmosphere and Climate of Mars* (Cambridge Univ. Press, 2017), pp. 106–171.

66. S. Maurice, B. Chide, N. Murdoch, R. D. Lorenz, D. Mimoun, R. C. Wiens, A. Stott, X. Jacob, T. Bertrand, F. Montmessin, N. L. Lanza, C. Alvarez-Llamas, S. M. Angel, M. Aung, J. Balaram, O. Beyssac, A. Cousin, G. Delory, O. Forni, T. Fouchet, O. Gasnault, H. Grip, M. Hecht, J. Hoffman, J. Laserna, J. Lasue, J. Maki, J. McClean, P.-Y. Meslin, S. Le Mouélic, A. Munguira, C. E. Newman, J. A. R. Manfredi, J. Moros, A. Ollila, P. Pilleri, S. Schröder, M. de la Torre Juárez, T. Tzanetos, K. M. Stack, K. Farley, K. Williford; SuperCam team, In situ recording of Mars soundscape. *Nature* **605**, 653–658 (2022).

67. M. E. Minitti, C. M. Weitz, M. D. Lane, J. L. Bishop, Morphology, chemistry, and spectral properties of Hawaiian rock coatings and implications for Mars. *J. Geophys. Res.* **112**, E05015 (2007).

68. R. F. Kokaly, R. N. Clark, G. A. Swayze, K. E. Livo, T. M. Hoefen, N. C. Pearson, R. A. Wise, W. M. Benzel, H. A. Lowers, R. L. Driscoll, A. J. Klein, "USGS Spectral Library Version 7" (Data Series Rep. 1035, USGS, 2017).

69. E. Cloutis, M. Craig, L. Kaletzke, K. McCormack, L. Stewart, HOSERLab, A new planetary spectrophotometer facility. *Lunar Planet. Sci.* **XXXVII**, 2121 (2006).

70. K. Kinch, M. Hilverda, M. B. Madsen, J. Bell, Calibrating Mars. *Planet. Rep.* **40**, 19–22 (2020).

Science Advances

Geological, multispectral, and meteorological imaging results from the Mars 2020 Perseverance rover in Jezero crater

James F. Bell, III, Justin N. Maki, Sanna Alwmark, Bethany L. Ehlmann, Sarah A. Fagents, John P. Grotzinger, Sanjeev Gupta, Alexander Hayes, Ken E. Herkenhoff, Briony H. N. Horgan, Jeffrey R. Johnson, Kjartan B. Kinch, Mark T. Lemmon, Morten B. Madsen, Jorge I. Nez, Gerhard Paar, Melissa Rice, James W. Rice, Jr., Nicole Schmitz, Robert Sullivan, Alicia Vaughan, Mike J. Wolff, Andreas Bechtold, Tanja Bosak, Louise E. Duflot, Alberto G. Fairn, Brad Garczynski, Ralf Jaumann, Marco Merusi, Chase Million, Eleni Ravanis, David L. Shuster, Justin Simon, Michael St. Clair, Christian Tate, Sebastian Walter, Benjamin Weiss, Alyssa M. Bailey, Tanguy Bertrand, Olivier Beyssac, Adrian J. Brown, Piluca Caballo-Perucha, Michael A. Caplinger, Christy M. Caudill, Francesca Cary, Ernest Cisneros, Edward A. Cloutis, Nathan Cluff, Paul Corlies, Kelsie Crawford, Sabrina Curtis, Robert Deen, Darian Dixon, Christopher Donaldson, Megan Barrington, Michelle Ficht, Stephanie Fleron, Michael Hansen, David Harker, Rachel Howson, Joshua Huggett, Samantha Jacob, Elsa Jensen, Ole B. Jensen, Mohini Jodhpurkar, Jonathan Joseph, Christian Juarez, Linda C. Kah, Oak Kanine, Jessica Kristensen, Tex Kubacki, Kristiana Lapo, Angela Magee, Michael Maimone, Greg L. Mehall, Laura Mehall, Jess Mollerup, Daniel Videz-Moreiras, Kristen Paris, Kathryn E. Powell, Frank Preusker, Jon Proton, Corrine Rojas, Danny Sallurday, Kim Saxton, Eva Scheller, Christina H. Seeger, Mason Starr, Nathan Stein, Nathalie Turenne, Jason Van Beek, Andrew G. Winhold, and Rachel Yingling

View the article online
https://www.science.org/doi/10.1126/sciadv.abo4856
Permissions
https://www.science.org/help/reprints-and-permissions

Use of this article is subject to the Terms of service